

Alma Mater Studiorum - Università di Bologna

**Scuola di Scienze
Corso di Laurea in Fisica**

X RAYS FROM LASER-PLASMA ACCELERATORS

Relatore:
Prof. Federico Boscherini

Presentata da:
Matteo Bischi

*Sessione III
Anno Accademico 2014/2015*

Abstract

One of the major goals of research for laser-plasma accelerators is the realization of compact sources of femtosecond x-rays. Relativistic interaction of short laser pulse with underdense plasmas has recently led to a novel generation of compact and femtosecond x-ray sources. These sources, based on radiation from electrons accelerated in plasma, have the common properties to be compact and to deliver collimated, incoherent and femtosecond radiation. In this thesis are presented some methods to obtain x-ray radiation from electrons accelerated with laser-plasma interaction: betatron radiation of trapped and accelerated electrons in the so-called bubble regime, synchrotron radiation of electrons in usual meter-scale undulators, and Thomson backscattered radiation. A review of the underlying physics, numerical simulations and some experimental results are presented for each mechanism. Finally, one of the most promising applications of laser-plasma accelerators is discussed: the free electron laser in the x-ray spectrum range, with intensities 10^8 - 10^{10} times greater than other laboratory sources.

Riassunto

Uno dei maggiori obiettivi della ricerca nel campo degli acceleratori basati su interazione laser-plasma è la realizzazione di una sorgente compatta di raggi x impulsati al femtosecondo. L'interazione tra brevi impulsi laser e un plasma, a energie relativistiche, ha recentemente portato a una nuova generazione di sorgenti di raggi x con le proprietà desiderate. Queste sorgenti, basate sulla radiazione emessa da elettroni accelerati nel plasma, hanno in comune di essere compatte, produrre radiazione collimata, incoerente e impulsata al femtosecondo. In questa tesi vengono presentati alcuni metodi per ottenere raggi x da elettroni accelerati per interazione tra laser e plasma: la radiazione di betatrone da elettroni intrappolati e accelerati nel cosiddetto "bubble regime", la radiazione di sincrotrone da elettroni posti in un onduttore convenzionale con lunghezza dell'ordine dei metri e la radiazione ottenuta dal backscattering di Thomson. Vengono presentate: la fisica alla base di tali metodi, simulazioni numeriche e risultati sperimentali per ogni sorgente di raggi x. Infine, viene discussa una delle più promettenti applicazioni fornite dagli acceleratori basati su interazione tra laser e plasma: il Free-electron laser nello spettro dei raggi x, capace di fornire intensità 10^8 - 10^{10} volte più elevate rispetto alle altre sorgenti.

01. Introduction

X-ray are a form of electromagnetic radiation, with wavelength ranging from 0.01 to 10 nanometres and energies from 100 eV to 100 keV. X-ray wavelengths are shorter than those of UV rays and longer than those of gamma rays.

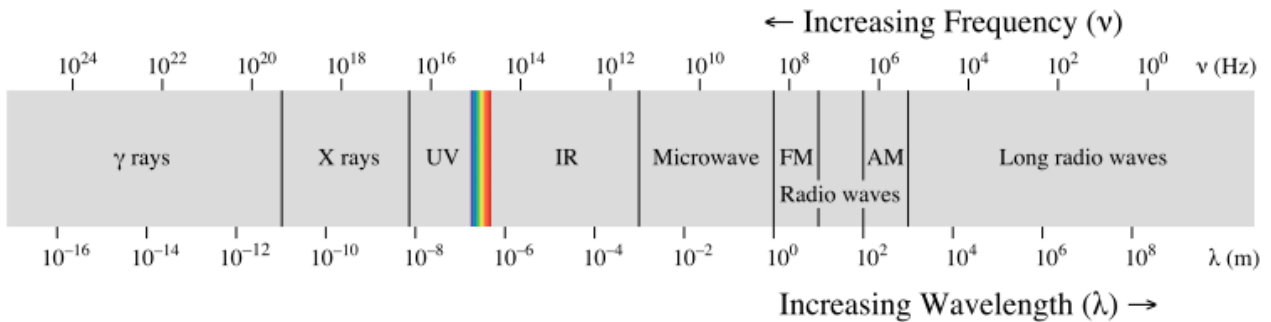


Fig.1.1. Electromagnetic radiation spectrum. *Reproduced from Wikipedia.*

X-rays have been one of the most effective tools used to explore the properties of matter for scientific research. Despite remarkable progress on x-ray generation methods, there is still a need for light sources, with micron size, delivering femtosecond pulses of bright high-energy x-ray and gamma-ray radiation, in order to provide the time resolution required to match the speed at which atomic-scale objects move. High-energy radiation can be delivered by radioactive sources, x-ray tube, and Compton scattering sources based on a conventional accelerator. These sources have limitation in terms of pulse duration, spectrum tunability and size.

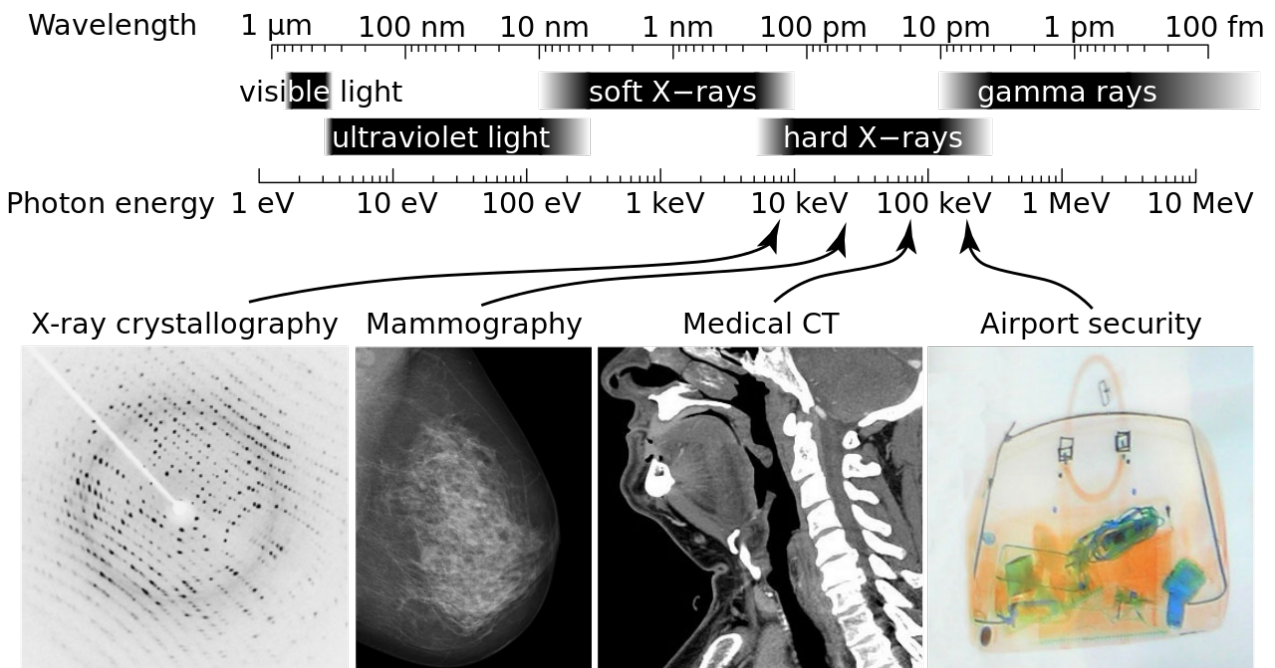


Fig. 1.2. X-ray applications. *Reproduced from Wikipedia*



Fig. 1.3.

An early X-ray picture (radiograph) taken at a public lecture by Wilhelm Röntgen of Albert von Kölliker's wife left hand on 23.1.1896
Reproduced from Wikipedia

With recent developments, laser systems can reach intensities above 10^{18} W/cm² and the laser-plasma interaction has entered the relativistic regime. Using laser-accelerated electrons, with relativistic energy, several new compact x-ray source schemes have been proposed to produce collimated and femtosecond radiation from the extreme ultraviolet to the gamma rays.

All these sources are based on the radiation from a relativistically moving charge (electron) and can be described using only five parameters:

- the relativistic factor $\gamma = 1/\sqrt{1 - \beta^2}$ of electrons
- the number of electrons N_e
- the strength parameter K
- the wavelength λ_e of the oscillating electron
- the number of periods N of the oscillating electron

The plan of this dissertation is the following. In the next part we have a theoretical introduction about radiation emitted from relativistic electrons and how we can accelerate electrons with the laser-plasma interaction up to relativistic energy. Then some methods are presented to produce x-rays or gamma-rays. The first one is a conventional undulator based on magnets (synchrotron radiation), the second one is based on a plasma undulator, then two electromagnetic wave undulators based on non-linear Thomson scattering and Thomson backscattering. Finally the free electron laser (FEL) is introduced, based on coherent radiation emitted by electrons interacting with their own radiation.

02. Radiation from relativistic electrons

Relativistic electrons can produce bright x-ray beams if their motion is appropriately driven. The features of this relativistically moving charge radiation are directly linked to the electron trajectories. The general expression that gives the radiation emitted by an electron, in the direction of observation \vec{n} , as a function of its position, velocity and acceleration along the trajectory can be written, in international units, as (Jackson, 2001)

$$\frac{d^2I}{d\omega d\Omega} = \frac{e^2}{16\pi^3 \epsilon_0 c} \cdot \left| \int_{-\infty}^{+\infty} e^{i\omega[t - \vec{n} \cdot \vec{r}(t)/c]} \frac{\vec{n} \times [(\vec{n} - \vec{\beta}) \times \dot{\vec{\beta}}]}{(1 - \vec{\beta} \cdot \vec{n})^2} dt \right|^2 \quad (1)$$

This equation represents the energy radiated within a spectral band $d\omega$ centred on the frequency ω and a solid angle $d\Omega$ centred on the direction of observation \vec{n} .

Here $\vec{r}(t)$ is the electron position at time t , $\vec{\beta}$ is the velocity of the electron normalized to the speed of light c , and $\dot{\vec{\beta}} = d\vec{\beta}/dt$ is the usual acceleration divided by c .

Observations:

- When $\dot{\vec{\beta}} = 0$ no radiation is emitted by the electron. This means that the acceleration is responsible for the emission of electromagnetic waves from charged particles.
- According to the term $(1 - \vec{\beta} \cdot \vec{n})^{-2}$, the radiated energy is maximum when $\vec{\beta} \cdot \vec{n} \rightarrow 1$. This condition is satisfied when $\beta \approx 1$ and $\vec{\beta} \parallel \vec{n}$. Thus, a relativistic electron will radiate orders of magnitude higher than a non relativistic electron, and its radiation will be directed along the direction of its velocity.
- The term $(\vec{n} - \vec{\beta}) \times \dot{\vec{\beta}}$ together with the relation $\dot{\beta}_{longitudinal} \propto \vec{F}_{longitudinal} / \gamma^3$ and $\dot{\beta}_{transvers} \propto \vec{F}_{transverse} / \gamma$ between applied force and acceleration, indicate that applying a transverse force $\vec{F} \perp \vec{\beta}$ is more efficient than a longitudinal force.
- The phase term $e^{i\omega[t - \vec{n} \cdot \vec{r}(t)/c]}$ can be approximated by $e^{i\omega(1-\beta)t}$. So the electron will radiate at the higher frequency $\omega = \omega_e / (1 - \beta) \approx 2\gamma^2 \omega_e$ where ω_e is the frequency of variation of the electron velocity $\vec{\beta}$. This indicates the possibility to produce x-ray beams by wiggling a relativistic electron beam at frequency far below the x-ray range $\omega_e = \omega_x / (2\gamma^2)$

The goal for x-ray generation from relativistic electrons is to force a relativistic electron beam to oscillate transversally. This transverse motion will be responsible for the radiation. This is the principle of synchrotron facilities, where a periodic static magnetic field, created by a succession of magnets, is used to induce a transverse motion to the electrons. The laser-based sources presented here rely on this principle.

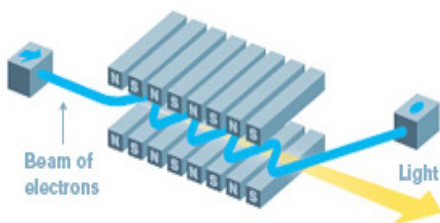


Fig. 2.1. Principle of emission of radiation from accelerated electrons. Reproduced from slac.stanford.edu

Two regimes of radiation can be distinguished: undulator and wiggler.

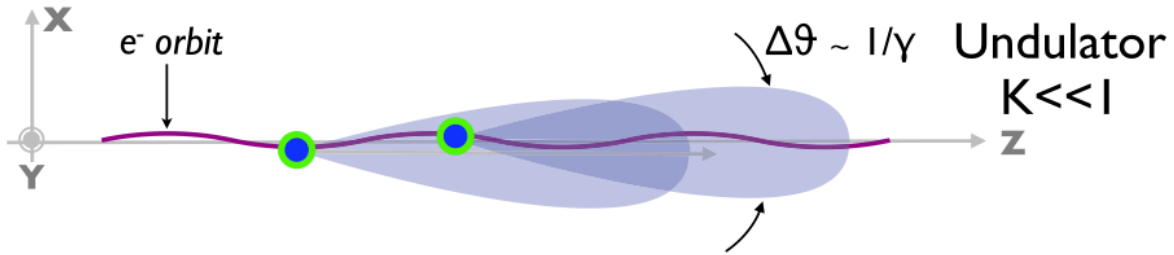


Fig. 2.2. Undulator regime. *Reproduced from Corde et al. (2013).*

The undulator regime corresponds to the situation where an electron radiates with the same opening angle in the forward direction along its motion. This occurs when the maximal angle of the trajectory Ψ is smaller than the opening angle of the radiation cone $\Delta\vartheta$.

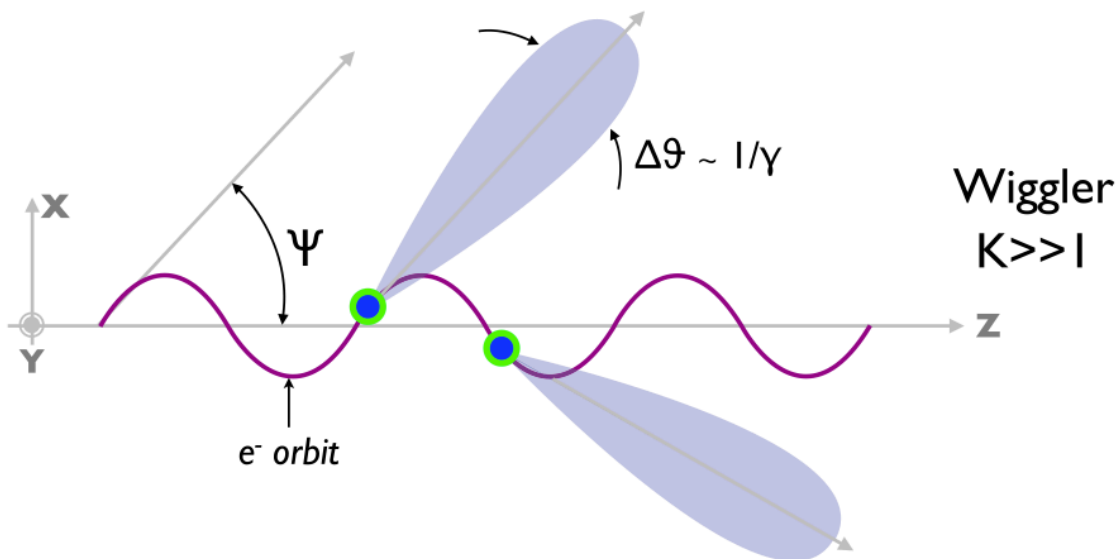


Fig. 2.3. Wiggler regime. *Reproduced from Corde et al. (2013).*

In the wiggler regime different sections of the trajectory radiate in different directions. This occurs when the maximal angle of the trajectory Ψ is bigger than the opening angle of the radiation cone $\Delta\vartheta$. The dimensionless parameter separating these two regimes is

$$K = \Psi / \Delta\vartheta = \gamma \cdot \Psi$$

The radiation produced in these two regimes have different qualitative and quantitative proprieties in terms of spectrum, divergence, radiated energy and number of emitted photons. It can be proved that:

$$\lambda \cong \frac{\lambda_u}{2\gamma^2} \left(1 + \frac{K^2}{2} + \gamma^2 \vartheta^2 \right) \quad (2)$$

Proof:

If the observation angle is zero ($\theta=0$) we have the situation represented in figure 2.4

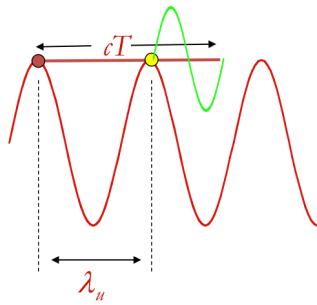


Fig. 2.4.

Constructive interference condition for a radiating electron. $\theta=0$

The red line is the electron trajectory and the green line represents the radiation emitted by the electron during its motion.

Reproduced from Boscherini's lecture notes (2015).

The emitted radiation wavelength (green line) is given by $\lambda = cT - \lambda_u$, where $T=S/v$ is the electron period, $v=c\beta$ is the electron velocity and $S = \lambda_u(1 + \frac{K^2}{4\gamma^2})$ is the distance travelled by the electron in a complete oscillation.

$$\lambda = c \frac{S}{c\beta} - \lambda_u = \lambda_u \left[\left(1 + \frac{K^2}{4\gamma^2}\right) \frac{1}{\beta} - 1 \right]$$

approximating $\frac{1}{\beta} \cong 1 + \frac{1}{2\gamma^2}$ we obtain $\lambda = \lambda_u \left[\left(1 + \frac{K^2}{4\gamma^2}\right) \left(1 + \frac{1}{2\gamma^2}\right) - 1 \right] \cong \frac{\lambda_u}{2\gamma^2} \left(1 + \frac{K^2}{2}\right)$

If the observation angle is not zero, the radiation wavelength is given by $\lambda = cT - \lambda_u \cos\vartheta$

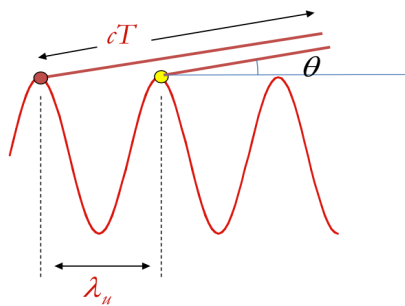


Fig. 2.5.

Constructive interference condition for a radiating electron. $\theta \neq 0$

The red line represents the electron trajectory.

Reproduced from Boscherini's lecture notes (2015).

$$\lambda = \lambda_u \left[\left(1 + \frac{K^2}{4\gamma^2}\right) \left(1 + \frac{1}{2\gamma^2}\right) - \cos\vartheta \right] \cong \frac{\lambda_u}{2\gamma^2} \left(1 + \frac{K^2}{2} + \gamma^2\vartheta^2\right)$$

With the trajectory of the electron periodic, the emitted radiation varies periodically during the process, because each time the electron is in the same acceleration state, the radiated amplitude is identical.

The radiation spectrum consists necessarily in the fundamental frequency $\omega = 2\pi c / \lambda$ and its harmonics. If $K \ll 1$ the spectrum consists in a single peak at the fundamental frequency ω .

If $K \gg 1$ the spectrum contains many harmonics of the fundamental, up to the critical frequency ω_c . An observer receives short burst of light of duration τ .

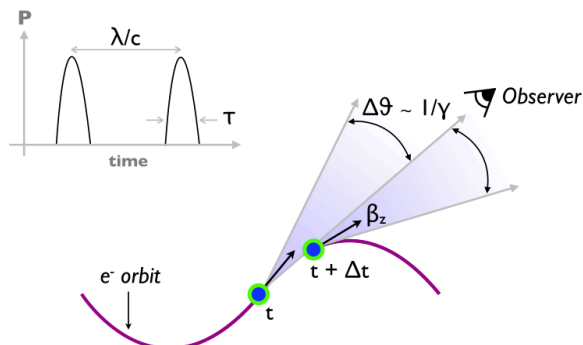


Fig. 2.6. Radiation emission during the electron motion.

Reproduced from Corde et al. (2013).

The parameter K can be considered as the number of decoupled sections of the trajectory. With each section radiating toward a different direction, the radiation is spatially decoupled and leads to bursts of duration τ in each direction and to a broad spectrum with harmonics up to ω_c . For an undulator, $K \ll 1$, the direction of the vector $\vec{\beta}$ varies along the trajectory by an angle Ψ negligible compared to $\Delta\vartheta = 1/\gamma$. Hence, the radiation from all sections of the trajectory overlap and the typical opening angle of the radiation is simply $\vartheta_r = 1/\gamma$.

For a wiggler, $K \gg 1$, in the direction of the motion \vec{e}_x , the typical opening angle of the radiation $\Psi = K/\gamma^2$ is greater than $\Delta\vartheta = 1/\gamma$; in the direction \vec{e}_y , the opening angle of the radiation is $\vartheta_{yr} = 1/\gamma$. Analytical calculations provide simple expression for the radiated energy per period (I_γ) and the number of emitted photons per period (N_γ).

$$I_\gamma = \frac{\pi e^2 \gamma^2 K^2}{3\epsilon_0 \lambda_u}$$

$$\text{For } K \ll 1 \quad N_\gamma = \frac{2\pi}{3} \alpha K^2$$

$$\text{For } K \gg 1 \quad N_\gamma = \frac{5\sqrt{3}\pi}{6} \alpha K$$

If we have N_e electrons contained in the bunch, assuming that they have exactly the same energy and initial momentum, the radiation is obtained by summing the contribution of each electron. If electrons are randomly distributed inside the bunch, radiation is incoherently summed, so

$$\frac{d^2 I}{d\omega d\Omega} = N_e \cdot \frac{e^2}{16\pi^3 \epsilon_0 c} \cdot \left| \int_{-\infty}^{+\infty} e^{i\omega[t - \vec{n} \cdot \vec{r}(t)/c]} \frac{\vec{n} \times [(\vec{n} - \vec{\beta}) \times \dot{\vec{\beta}}]}{(1 - \vec{\beta} \cdot \vec{n})^2} dt \right|^2$$

If the electron experiences the radiation from other electrons, this interaction of the bunch with its own radiation can lead to a microbunching of electron distribution. This is the free-electron laser (FEL) process which produces coherent radiation. Here the coherence factor is N_e^2 instead of N_e .

In the following sections, the interaction between electron bunch and its radiation will not be taken into account because in these schemes the condition required for the FEL are not fulfilled.

Electron acceleration in plasma

X-ray sources, which will be reviewed, are based on laser-plasma acceleration.

The basic concept of plasma acceleration and its possibilities were originally proposed by Tajima and Dawson of University of California, Los Angeles (UCLA) in 1979. The idea is to use the intense electric field of a relativistic plasma wave, created in the wake of an intense laser pulse, to accelerate electrons to relativistic energies. With this technology, electrons could be accelerated up to 1 GeV in millimeter or centimeter scale, while a few tens of meters would be necessary to reach the same energy in conventional accelerators. In late 2014, at the SLAC National Accelerator Laboratory, it was shown that laser-plasma interactions are able to achieve 400 to 500 times higher energy transfer compared to a general linear accelerator.

There are two important physical mechanisms: the ponderomotive force and the plasma wave. The ponderomotive force is a force associated with the intensity gradients in the laser pulse that pushes both electron and ions out of the high-intensity regions.

$$\vec{F}_p = -\frac{e^2}{4m\omega^2} \nabla \vec{E}^2$$

where m is the mass, E is the electric field and ω is the angular frequency on the field.

Ions, being much heavier than electrons, still remain for short interaction times, but electrons are cast away. The ponderomotive force of the laser pulse, which creates the initial charge density perturbation, leads to the formation of a relativistic plasma wave whose field can accelerate electrons. In practical units, the plasma wavelength λ_p and the laser strength parameter a_0 are given by

$$\lambda_p [\mu m] = 3.34 \cdot 10^{10} / \sqrt{n_e [cm^{-3}]}$$

$$a_0 = 0.855 \sqrt{I [10^{18} W / cm^2] \lambda_L^2 [\mu m]}$$

where I is the laser intensity, λ_L is the laser wavelength and n_e is the electron density.

Different plasma accelerator schemes have been developed over the years, but the most efficient is the so-called bubble wakefield regime. In that regime, electron bunches can be produced with tunable energy, low divergence and a bunch duration of less than 10 fs. This regime is reached if the waist w_0 of the laser pulse becomes matched to the plasma frequency ($\frac{\omega_p}{c} w_0 = 2\sqrt{a}$), if the pulse duration is of the order of half a plasma wavelength ($c\tau \approx \lambda_p / 2$) and if the laser intensity is sufficiently high ($a_0 > 2$) to expel most of the electrons out of the focal spot. If these conditions are met, an ion cavity is formed in the wake of the laser pulse.

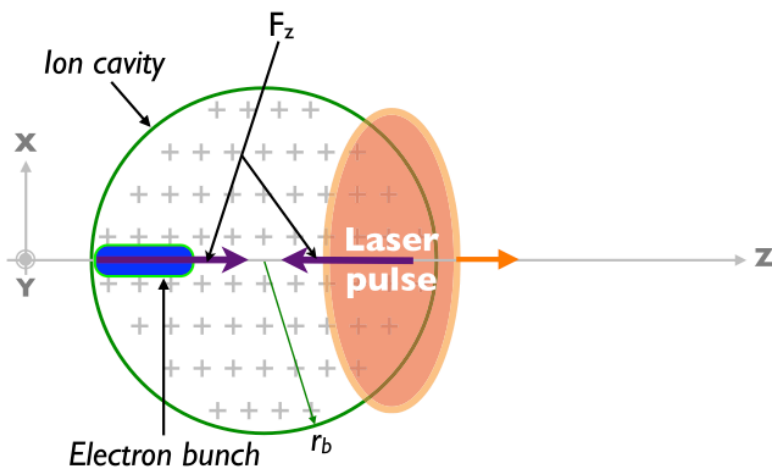


Fig. 2.7.
Electron acceleration in plasma.
Reproduced from Corde et al. (2013).

In figure 2.4 the principle of the electron acceleration in the bubble regime is shown. The laser pulse expels all plasma electrons out of the focal spot, creating an ion cavity in its wake. The longitudinal force F_z (produced by the electric field) accelerates the self-injected electron bunch in the first half of the bubble, while the bunch decelerates in the second half of the bubble. The distance over which electrons propagate before they reach that point is called the dephasing length L_d and is much larger than the bubble radius r_b . If the process is turned off at that time, electrons exit the plasma with the maximum energy gain.

03. Plasma accelerator and conventional undulator

Synchrotron radiation can be produced from laser-plasma accelerated electrons propagating and oscillating in a conventional undulator or wiggler. Electrons are first accelerated in a plasma accelerator and then transported into a conventional undulator or wiggler (a periodical structure of magnets generating a periodic static magnetic field).

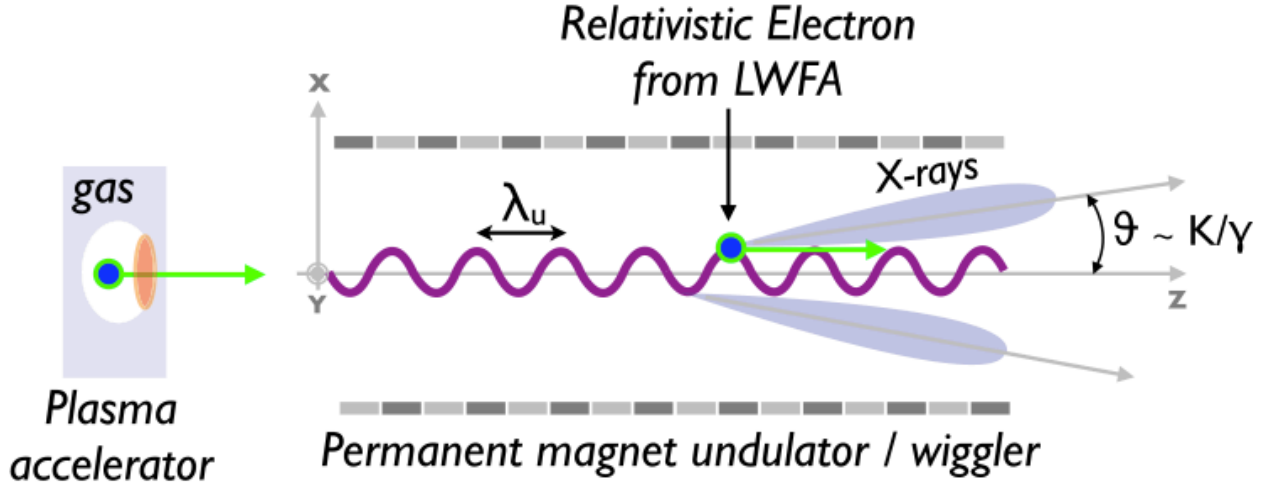


Fig. 3.1. Conventional undulator principle. Reproduced from Corde et al. (2013).

The size of this device is on the meter scale, with a typical magnetic period in the centimetre range. The value of λ_u is technologically limited, so GeV electrons are necessary to produce radiation in the x-ray range.

Electron motion

We consider a laser wakefield accelerator producing a monoenergetic electron bunch of energy $\varepsilon = \gamma mc^2$ with velocity directed in the \vec{e}_z axis. We can approximate the static magnetic field near the undulator axis by:

$$\vec{B} = B_0 \sin(k_u z) \vec{e}_y \quad \text{where} \quad k_u = 2\pi / \lambda_u$$

The equation of motion for a test electron is given by:

$$\frac{d\vec{p}}{dt} = -e\vec{v} \times \vec{B}$$

It can be proved that:
$$x(z) \cong -\frac{K}{\gamma k_u} \sin(k_u z) \quad \text{where} \quad K = \frac{eB_0}{k_u mc}$$

Proof:

If the magnetic field is in the \vec{e}_y direction and the velocity of the electron is in the \vec{e}_z direction, the Lorentz force is in the \vec{e}_x direction and it's given by $\vec{F} = e v_z B_0 \sin(k_u z) \vec{e}_x$

So,
$$m_0 \gamma \frac{dv_x}{dt} = e v_z B_0 \sin(k_u z) = e \frac{dz}{dt} B_0 \sin(k_u z)$$

Integrating, we obtain: $m_0\gamma v_x = -\frac{eB_0}{k_u}\cos(k_u z)$

So, $v_x = -\frac{eB_0}{k_u m_0 \gamma}\cos(k_u z) = -\frac{Kc}{\gamma}\cos(k_u z)$ where $K = \frac{eB_0}{k_u m_0 c}$

We can write the velocity as: $v_x = \frac{dx}{dt} = \frac{dx}{dz} \frac{dz}{dt} \cong c \frac{dx}{dz}$

So, $c \frac{dx}{dz} = -\frac{Kc}{\gamma}\cos(k_u z)$

And integrating we obtain: $x(z) \cong -\frac{K}{\gamma k_u}\sin(k_u z)$

The strength parameter K is determined by the amplitude of the magnetic field B_0 and the period λ_u and is, in practical units, given by: $K = 0.934 \lambda_u [cm] B_0 [T]$.

In particular K doesn't depend on γ and the radiation regime (undulator or wiggler) is the same for all electron energies.

Radiation properties

The spectrum of the emitted radiation depends on K. For a small amplitude of oscillation $K \ll 1$, radiation is emitted at the fundamental photon energy $\hbar\omega$ with a narrow bandwidth in the forward direction ($\vartheta = 0$). As $K \rightarrow 1$ harmonics of the fundamental start to appear in the spectrum, and for $K \gg 1$ the spectrum contains many closely spaced harmonics and extends up to a critical energy $\hbar\omega_c$.

These quantities are given (in practical units) by:

$$\hbar\omega [eV] = 2.48 \cdot 10^{-4} \gamma^2 / \lambda_u [cm] \quad \text{for } K \ll 1$$

$$\hbar\omega_c [eV] = 1.74 \cdot 10^{-4} \gamma^2 B_0 [T] \quad \text{for } K \gg 1$$

In the undulator regime, the radiation is collimated within a cone of typical opening angle $1/\gamma$. In the wiggler regime the radiation is collimated within an opening angle K/γ in the electron motion plane and $1/\gamma$ in the orthogonal plane.

The electron bunch duration depends on the acceleration mechanism and on its transport from its source to the undulator. Presently, the shortest electron bunches are obtained using a laser-driven plasma-based accelerator with an external optical injection mechanism. In this scheme, electron bunches with root mean square duration as small as 1.5 fs can be produced. In practical units, the number of photons emitted per period and per electron (at the mean photon energy $\langle \hbar\omega \rangle = 0.3\hbar\omega_c$ for the wiggler limit)

$$N_\gamma = 1.53 \cdot 10^{-2} K^2 \quad \text{for } K \ll 1$$

$$N_\gamma = 3.31 \cdot 10^{-2} K \quad \text{for } K \gg 1$$

Numerical results

In this section, the electron motion and the emitted radiation are calculated numerically (Corde et al., 2013). $K=0.2$ and $K=2$ are considered for undulator and wiggler case respectively. The magnetic structure has a period $\lambda_u=1$ cm and the test electron propagates in the \vec{e}_z direction with $\gamma=1000$. Figure 3.2 shows the electron orbit along 10 oscillations.

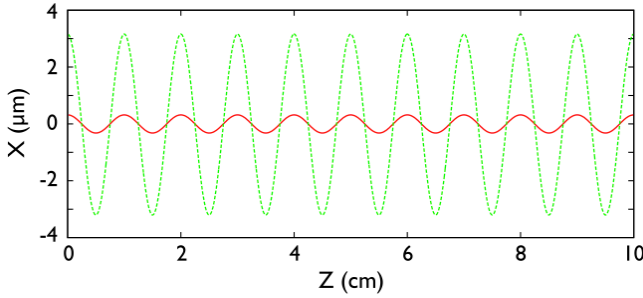


Fig. 3.2.

Electron trajectories. The red line represents the undulator case ($K=0.2$), the green line represents the wiggler case ($K=2$).

Reproduced from Corde et al. (2013).

The motion, with γ constant, consists of a transverse oscillation at a period λ_u combined with a longitudinal drift. For $K=0.2$ and $K=2$ the transverse amplitudes are $0.32 \mu\text{m}$ and $3.2 \mu\text{m}$, respectively. Figure 3.3(left) shows the spatial distribution of the radiation produced.

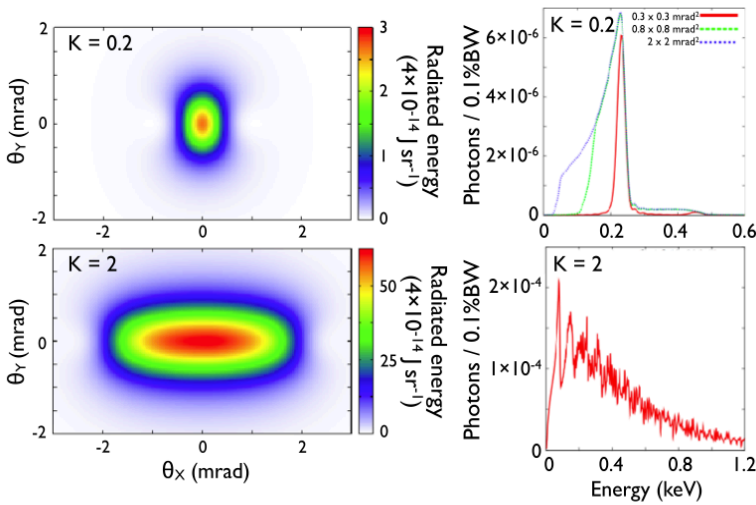


Fig. 3.3. On the left is represented the angular distribution of the radiation and the corresponding spectra are shown on the right.

The undulator case ($K=0.2$) is on the top. The wiggler case ($K=2$) is on the bottom.

Reproduced from Corde et al. (2013).

For $K=0.2$ (top), the radiation has a divergence of a typical opening angle $1/\gamma \sim 1$ mrad. For $K=2$ (bottom), the radiation has a divergence of a typical opening angle $K/\gamma \sim 2$ mrad in the plane of the electron motion and $1/\gamma \sim 1$ mrad in the orthogonal direction. The right part of the figure 3.3 represents the spectra of the emitted radiation for each situation. For the undulator case, the spectrum is plotted for three different solid angles of integration. The spectrum is nearly monochromatic at the energy of 200eV in the forward direction. For the wiggler case, the integration is performed over the total angular distribution. The spectrum becomes broadband with a critical energy of around 300 eV.

Experimental results

The first demonstration of the production of synchrotron radiation from laser-accelerated electrons was performed by Schlenvoigt et al. (2008). In this experiment, performed at the Jena University in Germany (with high-intensity titanium-sapphire laser JETI), laser-produced electron bunches between 55 and 75 MeV were injected into a 1 meter long undulator having a period $\lambda_u=2$ cm and a strength parameter $K=0.6$. They obtained synchrotron radiation in the visible and infrared part of the spectrum. This marks a noticeable step toward a new, compact, and brilliant short-wavelength light source.

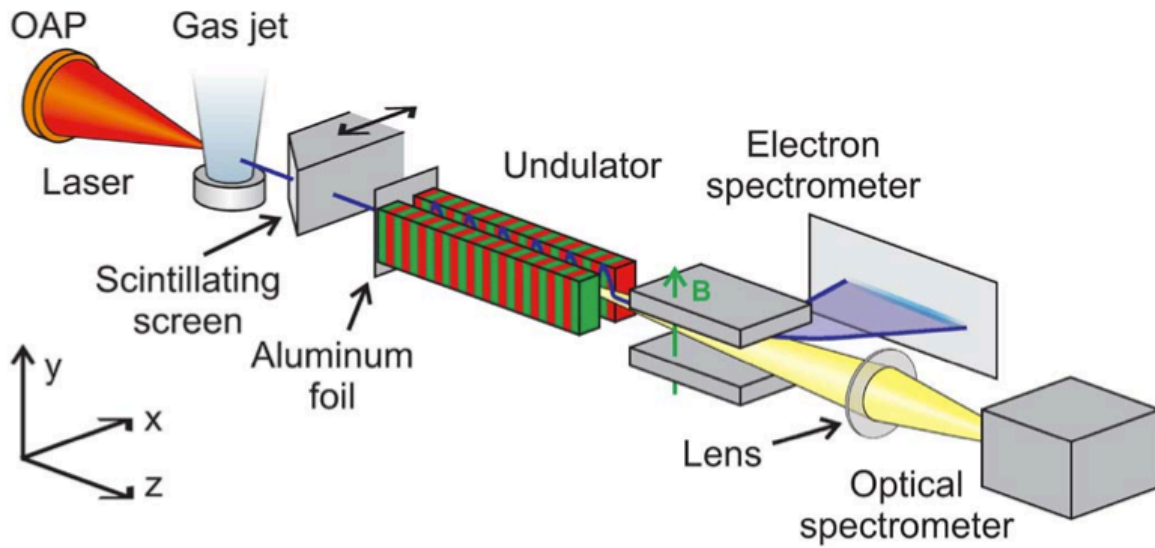


Fig. 3.4. Experimental setup. *Reproduced from Schlenvoigt et al. (2008)*

The setup of the experiment consists of an OAP (off-axis paraboloids) to focus the laser pulse, a laser-wakefield accelerator as electron source, electron beam diagnostics (scintillating screen), an undulator, an electron spectrometer, and an optical spectrometer. The spectrometer is protected against direct laser and plasma exposure by a thin aluminum foil placed at the undulator entrance. These parts were all aligned along the z-axis (direction of laser propagation). All parts, except the spectrometer were located inside vacuum chambers. An essential feature of the experiment is that the acceleration region, the electron spectrum, and the undulator-radiation spectrum were simultaneously recorded for each individual shot.

The relativistic laser-accelerated electrons undergo oscillations in the undulator perpendicular to the magnetic field and the propagation direction and, therefore, emit polarized radiation. Due to the relativistic movement, the emission is anisotropic and peaked in forward direction. The wavelength λ of the emitted light is mainly determined by the undulator period λ_u , and the electron energy $E_e = \gamma m_0 c^2$ and to the second order to the undulator parameter K, determining the amplitude of the oscillatory motion.

Furthermore, the emission wavelength depends on the angle of emission ϑ with respect to the propagation direction, as shown in formula (2).

For $K < 1$ as in the case of this undulator, the emitted wavelength in forward direction is approximately $\lambda \approx \lambda_u / 2\gamma^2$. For electron energies around 55-75 MeV, the wavelength of fundamental radiation emitted by our undulator ($\lambda_u = 2$ cm) is in the visible spectral range (560-990 nm). The energy E_u emitted by a single electron for fundamental undulator radiation ($n=1$) increases linearly with the numbers of periods N and quadratically with the electron energy γ .

$$E_u = \frac{\pi e}{3\epsilon_0} \frac{N\gamma^2 K^2 e}{\lambda_u (1 + K^2/2)^2}$$

Considering the mean photon energy $E_{ph} = hc / \lambda$, one can estimate the number of emitted photons per electron to be $N_{ph} = E_u / E_{ph}$. For more than one electron, the emission can superimpose coherently or incoherently. An incoherent superposition takes place if the

electrons are distributed over a distance significantly larger than the emitted wavelength λ . In that case, the number of emitted photons scales linearly with the number of electrons N_e . This is the situation of the experimental conditions described here.

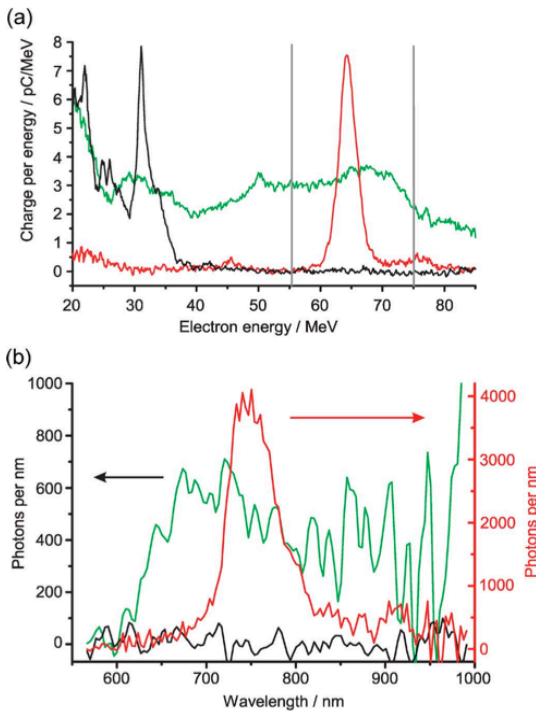


Fig. 3.5. Three examples of pairs of electron spectra (top) and corresponding optical-radiation spectra (bottom, same colour means same shot).
Reproduced from Schlenvoigt et al. (2008)

In figure 3.5 there are three examples of pairs of electron spectra (top) and corresponding optical-radiation spectra (bottom). The vertical gray bars in graph (a) indicate the range of electron energies (55-75 MeV) where undulator radiation would be within the range of the optical spectrometer (560-990 nm). The red electron spectrum is peaked at 64 MeV, right within the energy range of interest. We observe a very strong peak at 740 nm with the optical spectrometer (right-hand-side ordinate). The peak positions agree very well with the wavelength formula (2).

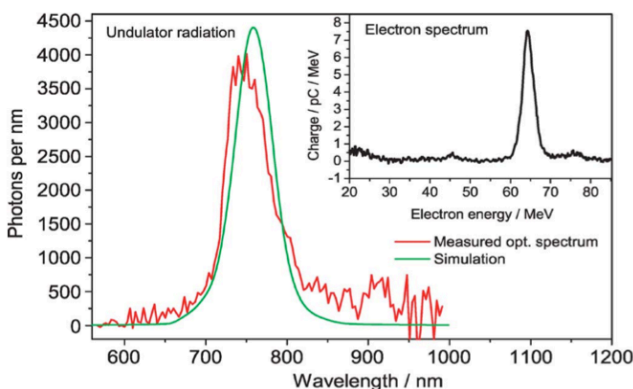


Fig.3.6. Measured optical-radiation spectrum (red) and simulated undulator-radiation spectrum (green)
Reproduced from Schlenvoigt et al. (2008).

Figure 3.6. shows an excellent agreement between the measured optical-radiation spectrum (red) and the simulated undulator-radiation spectrum (green) which was calculated from the corresponding electron spectrum.

04. Plasma accelerator and plasma undulator

As described in chapter 2, the laser-plasma interaction can create an ion cavity and can accelerate an electron bunch up to relativistic energy. In this method, the plasma cavity can act as a wiggler in addition to being an accelerator, reproducing, on a millimeter scale the principle of a synchrotron to produce x rays. In laser wakefield accelerators, the ponderomotive force of an intense femtosecond laser pulse generates, as it propagates in an underdense plasma, a large amplitude wakefield plasma wave. This wake can break, trap plasma electrons, and then its large electrostatic field can accelerate ultrashort pulse duration electron beams to high energies (a few hundreds of MeVs) on only a millimetre scale. A particularly efficient mechanism for wakefield generation occurs in the parameter regime corresponding to ultrashort laser pulses (~ 30 fs), called the forced laser wakefield regime, which has been studied experimentally and numerically. In this regime the wake has an electron-density depression right behind the laser pulse, leading to the formation of an ion column. This charge displacement results in a strong radial electrostatic field. As the relativistic electrons propagate through this fields, they can undergo oscillations, called betatron oscillations, at a frequency given by $\omega_b = \omega_p / \sqrt{2\gamma}$, where ω_p is the plasma frequency and γ the relativistic factor of the electron. This oscillatory relativistic transverse motion produces a collimated x-ray beam. This radiation, which can be directly compared to a synchrotron emission in the wiggler regime, is called betatron radiation. But, because the wavelength of the wiggler can be much shorted in a laser-plasma interaction (micron scale) than in a synchrotron based on fixed magnets (centimetre scale), the distance required to produce a bright x-ray beam is much shorter (on the scale of millimetres, rather than meter), the required energy of electron beam is much lower (MeV instead of GeV).

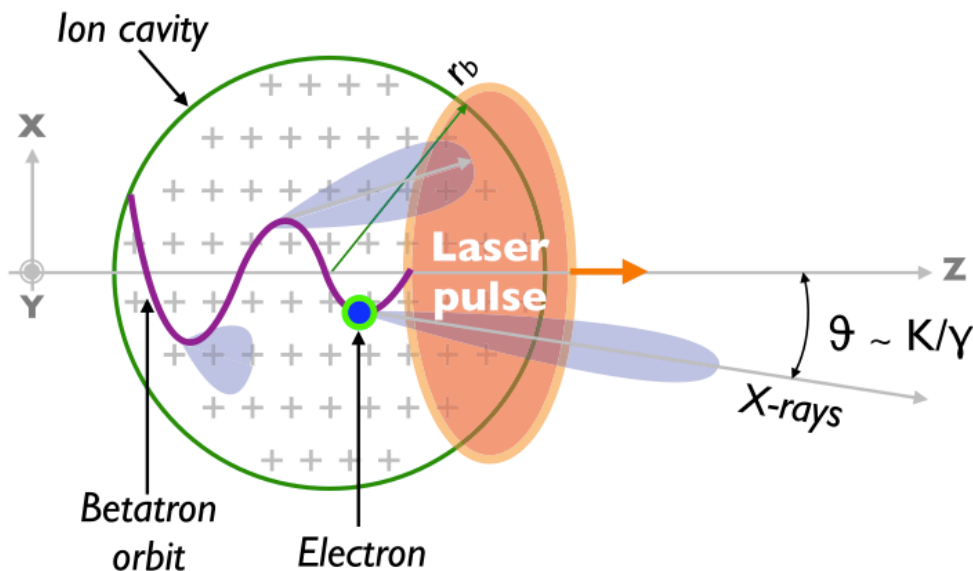


Fig. 4.1.
Plasma accelerator
and plasma
undulator principle.
*Reproduced from
Corde et al. (2013).*

Fig. 4.1 shows a representation of the principle of the plasma undulator. In addition to the longitudinal force, responsible for the acceleration discussed above, the spherical shape of the ion cavity results in a transverse electric field producing a restoring force directed toward the laser pulse propagation axis. So, when an electron is injected in the ion cavity, it is submitted not only to the accelerating force, but also to a restoring transverse force, resulting in its wiggling around the propagation axis.

Electron motion

In this section an idealized model of a wakefield in the bubble regime based on the phenomenological description developed by Lu, Huang, Zhou, Mori and Katsouleas (2006), Lu, Huang, Zhou, Tzoufras et al. (2006), and Lu et al. (2007) is considered.

The ion cavity is assumed to be a sphere of radius r_b . The equation of motion of a test electron in the cavity is then

$$\frac{d\vec{p}}{dt} = -e(\vec{E} + \vec{v} \times \vec{B}) = \vec{F}_{\parallel} + \vec{F}_{\perp}$$

The electron is initially injected at the back of the cavity with space-time coordinates $(t_i = 0, x_i, y_i, z_i)$ such that $x_i^2 + y_i^2 + z_i^2 = r_b^2$.

The term \vec{F}_{\parallel} is responsible for the electron acceleration in the longitudinal direction \vec{e}_z .

The term \vec{F}_{\perp} is a linear force that drives the transverse oscillation of the electron across the cavity axis at the betatron frequency $\omega_{\beta} \approx \omega_p / \sqrt{2\gamma}$, where $\omega_p = \sqrt{n_e e^2 / m \epsilon_0}$ is the plasma frequency. To derive the analytical expression of the electron orbit, we have to integrate the equation of motion from $t = 0$ to $t = \hat{t}$. The following expressions can be obtained:

$$\hat{x}(\hat{t}) = \hat{x}_{\beta}(\hat{t}) \cos\left(\int_0^{\hat{t}} \hat{\omega}_{\beta}(\hat{t}') d\hat{t}' + \varphi'_x\right)$$

$$\hat{y}(\hat{t}) = \hat{y}_{\beta}(\hat{t}) \cos\left(\int_0^{\hat{t}} \hat{\omega}_{\beta}(\hat{t}') d\hat{t}' + \varphi'_y\right)$$

$$\hat{\omega}_{\beta}(\hat{t}) = 1/\sqrt{2\gamma(\hat{t})}$$

$$\hat{x}_{\beta}(\hat{t}) = A'_x / \gamma(\hat{t})^{1/4}$$

$$\hat{y}_{\beta}(\hat{t}) = A'_y / \gamma(\hat{t})^{1/4}$$

The transverse motion consists of sinusoidal oscillations in each direction with time-dependent amplitude $\hat{x}_{\beta}(\hat{t})$, $\hat{y}_{\beta}(\hat{t})$ and frequency $\hat{\omega}_{\beta}(\hat{t})$. The betatron amplitudes decrease as $\gamma^{-1/4}$ during acceleration, while the betatron frequency decreases as $\gamma^{-1/2}$. This trajectory is noticeably different from the one studied for a conventional undulator. First, the betatron amplitude and frequency are time dependent. Second, $x(t)$ and $y(t)$ are sinusoidal functions of t and not z . Even if the detail of electron dynamics is slightly different from the previous case, the betatron trajectory has the same properties.

In the equation of motion, the electromagnetic field corresponds to an idealized cavitated regime. It assumes three conditions: (i) the matching conditions in terms of focal spot size, laser pulse duration, and density are perfectly met; (ii) the cavity is free of electrons; and (iii) the trapped electrons are only submitted to the wakefields (there is no interaction with the electromagnetic field of the laser pulse). In addition, in this approach, initial conditions have to be arbitrarily chosen since the injection mechanism is not taken into account.

Radiation properties

The betatron motion derived in the above simple model leads to the emission of synchrotron radiation referred to as betatron radiation. It can be calculated within the general formalism of the radiation from a moving charge. The ion cavity acts as an undulator or a wiggler with period $\lambda_u(t)$ and strength parameter $K(t)$ which depends on the electron initial conditions upon injection into the cavity. We first consider the radiation properties for constant λ_u , K and γ and then consider the radiation produced by the electron with acceleration.

- Without acceleration

The spectrum of the emitted radiation depends on the amplitude of K . For a small amplitude of the betatron oscillation $K \ll 1$, the radiation is emitted at the fundamental photon energy $\hbar\omega$ with a narrow bandwidth in the forward direction ($\vartheta = 0$). As $K \rightarrow 1$ harmonics of the fundamental start to appear in the spectrum, and for $K \gg 1$ the spectrum contains many closely spaced harmonics and extend up to a critical energy $\hbar\omega_c$.

These quantities are given by

$$\begin{aligned} \hbar\omega &= (2\gamma^2 hc / \lambda_u) / (1 + K^2 / 2) && \text{for } K \ll 1 \\ \hbar\omega_c &= \frac{3}{2} K \gamma^2 hc / \lambda_u && \text{for } K \gg 1 \end{aligned}$$

The radiation is collimated within a cone of typical opening angle $1/\gamma$ in the undulator case. For a wiggler, the radiation is collimated within a typical opening angle K/γ in the electron motion plane and $1/\gamma$ in the orthogonal plane. The x-ray pulse duration equals the electron bunch duration. Depending on the parameters and the electron injection process, it can be extremely short, a few fs, corresponding to a bunch length equal to a very small fraction of the bubble radius, or using massive self-injection at high density, the bunch length can be on the order of the bubble radius. The number of emitted photons can be estimated using expressions:

$$\begin{aligned} N_\gamma &= 1.53 \cdot 10^{-2} K^2 && \text{for } K \ll 1 \\ N_\gamma &= 3.31 \cdot 10^{-2} K && \text{for } K \gg 1 \end{aligned}$$

- With acceleration

For electron accelerating, the situation is more complex. We consider the wiggler limit and we derive an approximation for the radiation spectrum taking into account the acceleration. The acceleration has a characteristic parabolic profile $\gamma(\tau) = \gamma_d(1 - \tau^2)$, with $\tau = (\hat{t} - \hat{t}_d) / \sqrt{\hat{t}_d^2 + 8\gamma_\phi^2 \gamma_i}$ and \hat{t}_d the dephasing time. It is possible to obtain the following expressions:

$$\omega_\beta(\tau) = \omega_{\beta,d} (1 - \tau^2)^{-1/2}$$

$$K(\tau) = K_d (1 - \tau^2)^{1/4}$$

$$\hbar\omega_c(\tau) = \hbar\omega_{c,d} (1 - \tau^2)^{7/4}$$

$$\bar{P}_\gamma(\tau) = \bar{P}_{\gamma,d} (1 - \tau^2)^{3/2}$$

where $\omega_{\beta,d}$, K_d , $\hbar\omega_{c,d}$ and $\bar{P}_{\gamma,d}$ are the values of the parameters at the dephasing time $\tau=0$, and $\bar{P}_{\gamma}(\tau)$ is the radiated power averaged over one oscillation period. We consider that the spectrum radiated per unit time is a synchrotron spectrum and is given by $dP/d\omega = (\bar{P}_{\gamma}/\omega_c)S(\omega/\omega_c)$, which is exact for a helical trajectory but only approximate for a sinusoidal trajectory. The radiation spectrum then reads

$$\frac{dI}{d\omega} \approx \frac{\bar{P}_{\gamma,d} t_d}{\omega_{c,d}} S'(\omega/\omega_{c,d})$$

where the function S' is defined as $S'(x) = \int_{-1}^0 \frac{d\tau}{(1-\tau^2)^{1/4}} S[(1-\tau^2)^{-7/4} x]$

The shape of the spectrum is not described by the usual universal function S of the synchrotron spectrum anymore, but by the function S' defined above.

Numerical results

In this section, the case of an electron experiencing the longitudinal acceleration force is treated numerically (Corde et al. 2013). The orbit of a test electron in the ion cavity can be obtained integrating the equation of motion. The electron density is $n_e = 1 \cdot 10^{19} \text{ cm}^{-3}$, the propagation length is set at 1.2 mm and the laser strength parameter is $a_0 = 4$ (only used to calculate the bubble radius $r_b = 6.72 \mu\text{m}$). The test electron enters at the back of the cavity with $x_i = 2 \mu\text{m}$, $y_i = 0$, $z_i = -6.42 \mu\text{m}$, and $p_{xi} = 0$, $p_{yi} = 0$, $p_{zi} = 25mc$. The trajectory obtained is shown in figure 4.2.

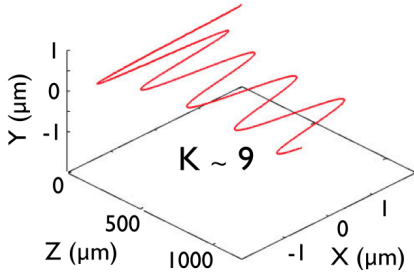


Fig. 4.2.
Electron trajectory in the ion cavity.
Reproduced from Corde et al. (2013).

Figure 4.3 shows the γ factor as a function of the longitudinal coordinate z . The electron is rapidly accelerated and acquire an energy up to ~ 240 MeV. It is decelerated after the dephasing length has been reached.

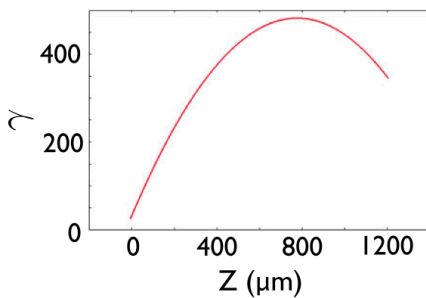


Fig.4.3.
Gamma factor as a function of the longitudinal coordinate z .
Reproduced from Corde et al. (2013)

As discussed before, the acceleration field may be largely overestimated and several effects not taken into account here can affect the acceleration process. Thus, the predicted maximum electron energy can be largely overestimated in this test-particle simulation.

The radiation has been calculated using the general formula:

$$\frac{d^2I}{d\omega d\Omega} = \frac{e^2}{16\pi^3 \epsilon_0 c} \left| \int_{-\infty}^{+\infty} e^{i\omega[t - \vec{n} \cdot \vec{r}(t)/c]} \frac{\vec{n} \times [(\vec{n} - \vec{\beta}) \times \dot{\vec{\beta}}]}{(1 - \vec{\beta} \cdot \vec{n})^2} dt \right|^2$$

in which the orbit calculated above is included.

Figure 4.4 represents the spatial distribution of the radiated energy that is a signature of the transverse electron orbits in the cavity.

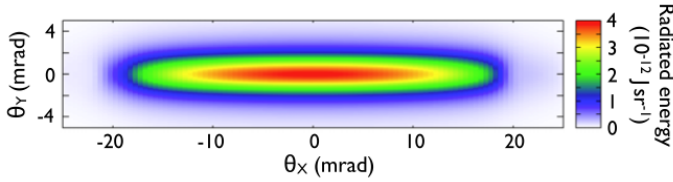


Fig.4.4.

Spatial distribution of the radiated energy.

$\vartheta_x \sim 18\text{mrad}$ and $\vartheta_y \sim 2\text{mrad}$

Reproduced from Corde et al. (2013)

The shape of the trajectory is determined by the initial conditions (x_i, y_i, z_i) and (p_{xi}, p_{yi}, p_{zi}) and can be planar (as presented here), circular or helical. As an example, the spatial distribution of the radiation produced by an electron undergoing two types of transverse orbits are represented in figure 4.5

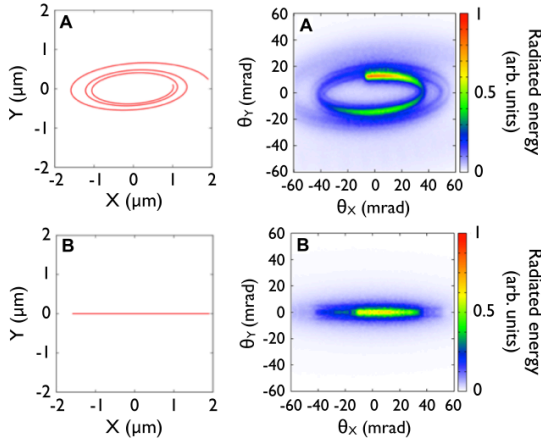


Fig.4.5.

Transverse trajectory (on the left) and angular profile of the corresponding emitted radiation (on the right).

The trajectory is three dimensional and helical in case A, and is planar in case B.

Reproduced from Corde et al. (2013)

Now we look at a particle-in-cell (PIC) simulation, taking into account all possible effects in a typical experimental parameters range. The macroparticles, each representing an assembly of electrons, evolve in a full 3D space. Monitoring macroparticle trajectories gives us the same information as a test-particle code, but with realistic wakefield, energies, and injection properties in space and time. As soon as particle energy reaches 45 MeV, it is considered as being injected and we keep track of its trajectory for the rest of the simulation time. The simulation ends when the particles come out of the plasma. Approximately 10^5 macroparticles are tracked, and their three position coordinates and their γ factor are recorded every 5 fs. To reduce the computing time, it is possible to use the synchrotron radiation formula, since betatron radiation occurs in the wiggler regime. The angle-dependent spectrum $d^2I/d\omega d\Omega$ can also be obtained in the wiggler limit by using the “saddle point” method. The saddle points are defined as the points in the electron trajectories where the velocity vector \vec{v} is parallel to a given observation direction \vec{n} . The total radiation spectrum is then obtained as the sum of the synchrotronlike burst of all saddle points. The simulation describes all the steps of the bubble regime: penetration of laser pulse in the plasma, formation of the bubble, injection of electrons at the back of the bubble and acceleration, wiggling of the electron bunch in the bubble, laser energy depletion, and scattering of the bunch in the plasma when it comes out of

the focusing transverse electric field of the bubble. All these steps are represented in figure 4.6.

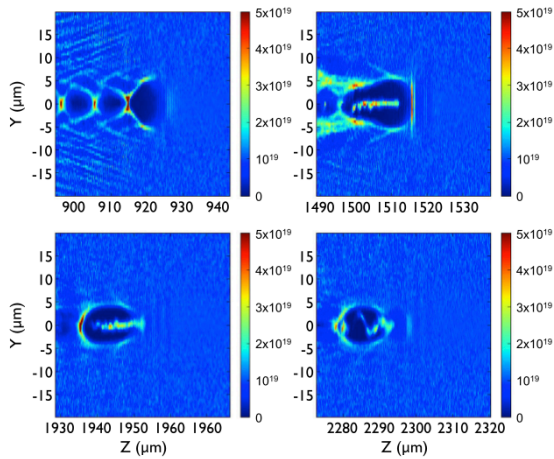


Fig.4.6. Electron density in the z-y plane averaged over 5 μm in the x direction. Densities are given in cm^{-3} and are represented by the colour scale on the right. The four images are taken at four different times and four different positions along the z axis. First the bubble forms, then injection starts, a whole bunch of accelerated electrons is created inside the bubble, and finally the bunch comes out of the bubble and is scattered.
Reproduced from Corde et al. (2013)

Figure 4.7 shows the electron beam spectrum before scattering. Most of the electrons are around 100 MeV but the tail extend up to 350 MeV.

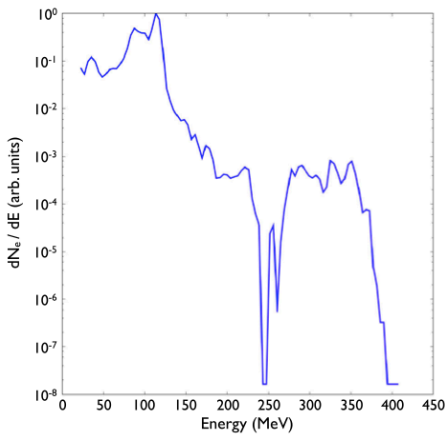


Fig. 4.7. Normalized electron beam spectrum before scattering at $z \approx 1800 \mu\text{m}$.
Reproduced from Corde et al. (2013)

Figure 4.8 focuses on a single particle. It illustrates the fact that a particle in the bunch, first accelerated and then dephased, follows a sinusoidal orbit around the propagation axis and radiates the most when it has both a high γ and a strong perpendicular acceleration.

Figure 4.9 shows typical trajectories of electrons during their acceleration inside the bubble in the polarization plane. Each line represents the trajectory of one macroparticle in the code. The colour of a line changes as the macroparticle is accelerated to higher energy (according to the relativistic γ factor).

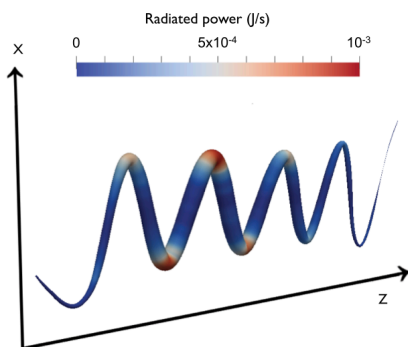


Fig. 4.8. Trajectory, energy and radiated power of a single electron before scattering. The thickness of the line is proportional to the particle's energy and the colour measures the instantaneous radiated power of the particle.
Reproduced from Corde et al. (2013)

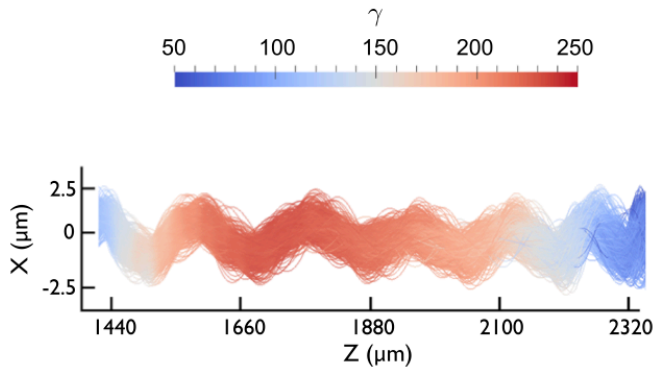


Fig. 4.9.
Trajectories of 500 electrons, from injection until scattering, with the same initial conditions.
Reproduced from Corde et al. (2013)

Figure 4.10 shows trajectories and radiated power of the same particles. As expected, most of the radiation is produced inside the bubble at high electron energies and far from the axis, where the transverse acceleration is the highest.

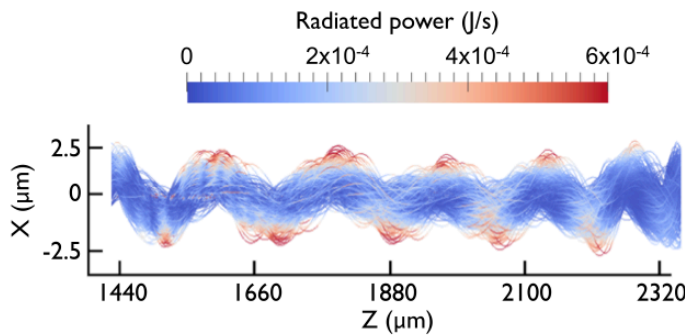


Fig. 4.10.
Trajectories and radiated power of the same 500 particles of figure 4.9.
Reproduced from Corde et al. (2013)

Radiation is emitted in the direction of the electron velocity. Figure 4.11 shows the angular distribution of the radiated energy. It is very well centred on the propagation axis and has an angular width of 30 mrad (FWHM).

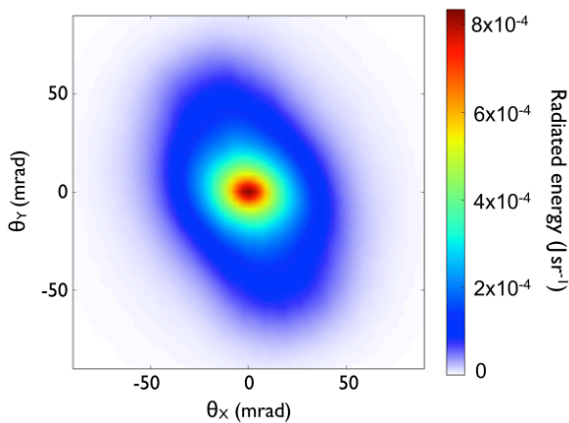
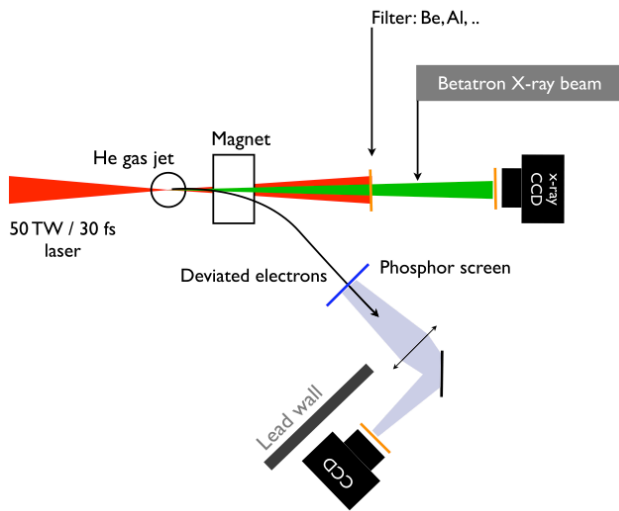


Fig. 4.11.
Angular profile of the emitted radiation
Reproduced from Corde et al. (2013)

Experimental results

The first experiment based on a fully laser-plasma approach discussed above was performed at the Laboratoire d'Optique Appliquée by Rousse et al. (2004) using a titanium-doped sapphire laser operating at 10 Hz with a wavelength of 820 nm, focused onto a 3 mm helium gas jet at an electron density of $\sim 10^{19} \text{ cm}^{-3}$. A typical betatron experimental setup is shown in figure 4.12.



4.12.

Experimental setup for the generation and observation of betatron radiation.
Reproduced from Corde et al. (2013)

An intense femtosecond laser pulse is focused onto a supersonic helium gas jet. Electrons accelerated during the interaction are deflected toward a phosphor screen using a permanent magnet with the field of ~ 1 T. Because the magnet bends the electron trajectories in only one direction, the image on the screen reveals the electron spectrum and the beam divergence. The x-ray radiation is observed using an x-ray CCD placed on axis. The experimental results are found to be in good agreement with the numerical simulation and the analytical estimations describing the radiation emitted by the trapped electrons undergoing betatron oscillation in the ion channel. The total number of photons integrated over the bandwidths of the filters is more than 10^8 photons, per shots and integrated over all angles, which is in good agreement with the simulation. The radiation is found to be collimated in a narrow cone centered on the laser axis and the divergence increases with the electron density.

Figure 4.13 shows the angular distribution of the radiation for x-ray energies beyond 1 keV. A) The measurement is made for $n_e=10^{19}$ cm $^{-3}$. Each point corresponds to an average value over ten shots. The dotted line represents the result obtained from the 3D PIC simulation. B) Spatial profile of the x-ray beam at $n_e=8 \cdot 10^{18}$ cm $^{-3}$.

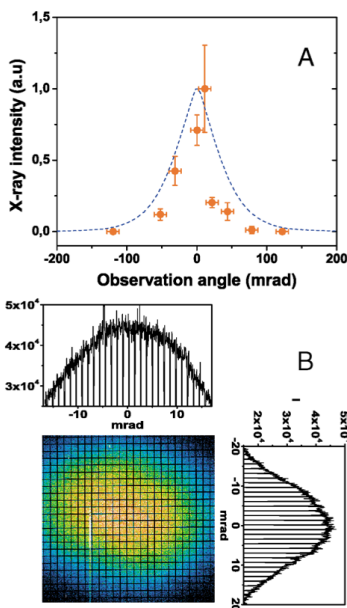


Fig. 4.13

Angular distribution of the radiation for x-ray energy beyond 1 keV
Reproduced from Rouse et al. (2004).

The x-ray beam divergence, averaged over more than ten shots, is found to be $\Delta\theta=(50\pm 20)$ mrad. It is found that the betatron radiation has a specific dependence with plasma density. Figure 4.14 shows that the radiative process is more efficient at the plasma density $n_{e\max}=1.1 \cdot 10^{19}$ cm $^{-3}$ at which the x-ray intensity is sharply peaked. The PIC numerical

simulations clearly reproduce this experimental behavior. Below $5 \times 10^{18} \text{ cm}^{-3}$, the x-ray signal vanishes because no electron is trapped. Just above this threshold, electrons are trapped in the bubble regime and monoenergetic electron bunches as well as betatron radiation of relatively low intensity can be obtained. When the density is higher, the plasma wavelength is smaller and the focal spot size and pulse duration are not exactly matched.

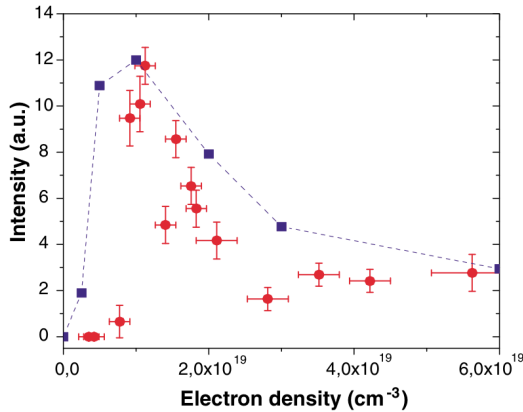


Fig. 4.14

X-ray signal as a function of the plasma electron density for x-ray energies beyond 1 keV. Each point correspond to an average value over ten shots. The dotted line corresponds to the result obtained using 3D PIC simulation.

Reproduced from Rousse et al. (2004)

Three typical spectra, which can be obtained simultaneously with the measurement of betatron radiation, are represented in figure 4.15. The first shows a broad band spectrum obtained at relatively high density, the second corresponds to a monoenergetic electron bunch (signature of the bubble regime) obtained for a density just above the trapping threshold, the third is obtained for a density below this threshold and no electron is observed.

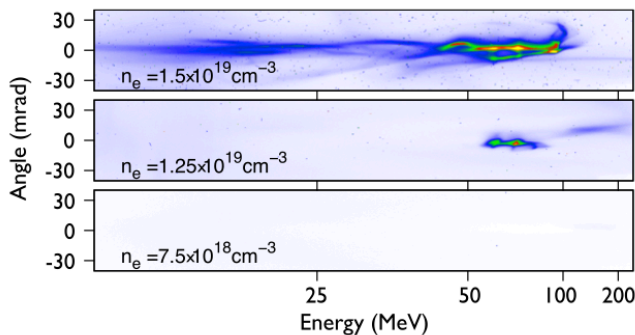


Fig. 4.15

Electron spectra for three different densities and fixed laser parameters. The number of counts is indicated by the colour scale (from blue to red).

Reproduced from Corde et al. (2013)

The spectrum of the betatron radiation was first measured using a set of filters, for an electron density $n_e = 1 \cdot 10^{19} \text{ cm}^{-3}$. Figure 4.16 presents the number of x-ray photons obtained experimentally, integrated over the beam divergence and over the spectral bandwidths determined by three filters: $25 \mu\text{m Be}$ ($1 < E < 10 \text{ keV}$), $25 \mu\text{m Be} + 40 \mu\text{m Al}$ ($4 < E < 10 \text{ keV}$) and $25 \mu\text{m Be} + 25 \mu\text{m Cu}$ ($6 < E < 10 \text{ keV}$).

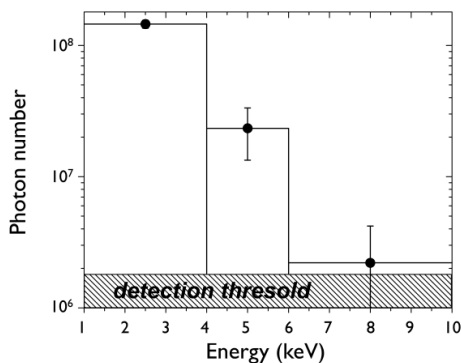


Fig. 4.16.

Total number of photons obtained experimentally within the spectral bandwidth determined by three filters.

Reproduced from Rousse et al. (2004)

Recently the electron bunch duration was measured with a root-mean-square of 1.5 fs (Lundh et al. 2011). Betatron radiation was shown to be strongly correlated with the properties of

these electron bunches, so even radiation has duration of a few femtoseconds. The source size is in the range of $\sim 1\text{-}2\ \mu\text{m}$.

Betatron x-ray radiation has interesting properties for application experiments: high peak spectral brightness, ultrashort duration, very small source size, as well as femtosecond time-scale synchronization in pump-probe experiments. The potential of betatron radiation was demonstrated by Fourmaux et al. in 2011 with some examples of single shot phase contrast imaging. In figure 4.17 some nylon wires with diameters between 10 and 330 μm were used.

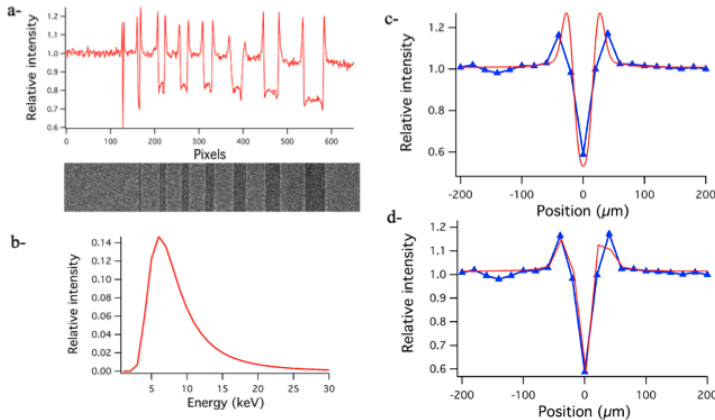


Fig. 4.17.

(a) Nylon wires imaged by the Betatron x-ray beam and lineout. (b) Spectrum used for the calculation. (c) and (d) Comparison of measurement (blue triangles) and calculation (red solid curve) for a 4 μm x-ray source.

(d) The 20 μm CCD pixel size is taken into account.

Reproduced from Fourmaux et al 2011a.

Figure 4.18(a) shows a more complex and thick object: a bee located 94.5 cm from the x-ray source and imaged in air with one single shot Betatron x-ray pulse. In the bee plane, the field of view is 19 x 19 mm^2 and the resolution is 15 μm . The same bee with an accumulation of 13 pulses is shown on figure 4.18(b).

In single shot, the contrast value is 0.68, while with 13 shots it is reduced to 0.48. The contrast value is defined as the ratio between the luminance difference and the average luminance. The luminance is a photometric measure of the luminosity intensity per unit area.

$$\text{Contrast} = \frac{I_{\max} - I_{\min}}{(I_{\max} + I_{\min})/2}$$

However, very thin details can be observed in single shot, but disappear in multishots because of a loss of resolution. In conclusion, a phase contrast image of a bee can be recorded using the betatron x-ray beam produced by a single laser pulse. This clearly demonstrates the potential of the betatron x-ray beam for biomedical applications, allowing tomography of small complex objects in less than a minute or imaging an object by x-ray phase contrast in real time at 10 Hz repetition rate.

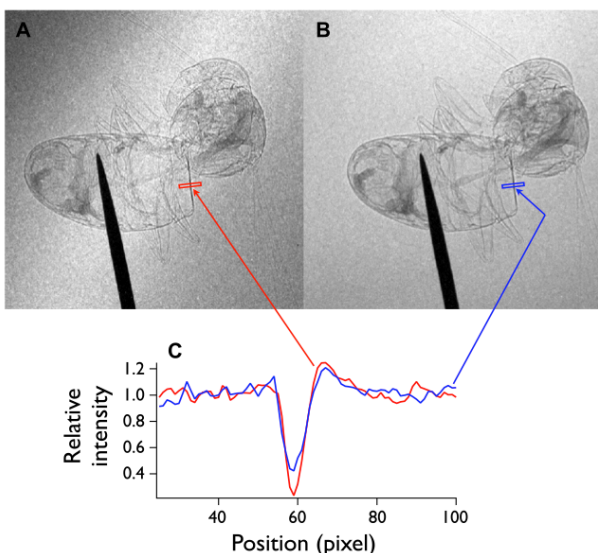


Fig. 4.18.

Bee imaged with the x-ray betatron beam with an edge line out indicated by the rectangular area: (a) 1 laser shot; (b) 13 laser shots.

Reproduced from Fourmaux et al 2011a.

05. Electromagnetic wave undulator

In this section, the production of x-ray and gamma-ray beams from electrons oscillating in an electromagnetic wave is reviewed. The radiative mechanism is Compton scattering. When the electron experiences a negligible recoil in the electron rest system (which happens when $\hbar\omega \ll m_e c^2$), the mechanism is called Thomson scattering, the low-energy limit of Compton scattering. In the following we consider Thomson scattering and use a classical description: it corresponds to the absorption of one or several photons by an electron and to the emission of a single photon. In the first case the mechanism is called linear Thomson scattering, in the second case it is called nonlinear Thomson scattering. Two schemes of femtosecond x-ray or gamma-ray sources based on Thomson scattering have been proposed (using laser-plasma acceleration). Based on the same principle, the two methods differ by the initial energy of the electron and the intensity of the laser pulse scattering off the electrons. In the first scheme, electrons are initially at rest and laser wakefield acceleration is not invoked. Here Thomson scattering occurs in highly nonlinear regime. For $a_0 \gg 1$, electrons have a highly nonlinear motion and the emitted radiation consists of high-order harmonics. The harmonic spectrum can extend up to the x-ray range. However, reaching the keV energy range requires very high laser strength parameters, typically $a_0 > 10$. The second scheme consists on Thomson scattering an intense laser pulse off a counter-propagating relativistic electron beam. This scheme offers the possibility to produce x-rays in the keV range even with modest electron energy (tens of MeV) or gamma rays if 100 MeV range electrons are used. In the following sections (A and B) the two schemes are discussed. For both, electron orbits, radiation properties, numerical and experimental results are presented.

A) Nonlinear Thomson scattering

The production of femtosecond x-ray radiation from electrons initially at rest is discussed. In this method, Thomson scattering occurs in a strongly nonlinear regime and electrons are directly accelerated and wiggled with an intense laser field. The number of electrons involved in the emission process can be much larger than the number of electrons trapped and accelerated in a laser-plasma accelerator, so this method offers the possibility to produce a large photon flux. However, producing x-ray radiation requires a laser strength parameter a_0 much greater than unity. In this regime ($a_0 \gg 1$) the term $-e\vec{v} \times \vec{B}$ of the Lorentz force, negligible at low intensity, becomes comparable to the $-e\vec{E}$ component and the motion is a nonlinear function of the driving field in addition to becoming relativistic. The electron motion is no longer harmonic and the radiation emitted consists of high-order harmonics forming a broadband spectrum that extends up to the x-ray range. The spectrum shifts to higher energies as a_0 increases. This radiative mechanism is called nonlinear Thomson scattering. Figure 5.1 shown the principle of this source. It simply consists of focusing an intense laser on a target (in this case the target is an underdense plasma).

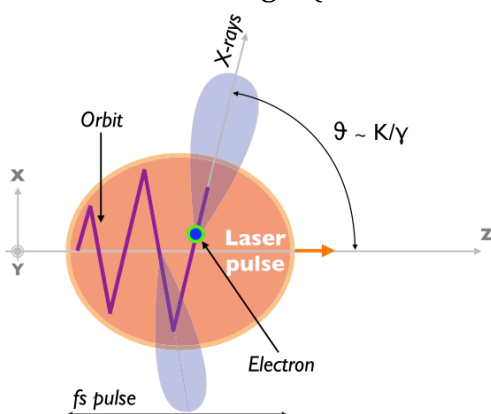


Fig. 5.1.

Principle of nonlinear Thomson scattering.

This illustrates the motion of an electron in the case of a linearly polarized laser pulse.

Reproduced from Corde et al. (2013).

Electron motion

The electron orbit is derived in the case of a circularly polarized laser pulse, because it leads to a situation where the concept of wiggling, developed in the section 2, can be applied.

A test electron initially at rest ($\gamma_i = 1$) and submitted to an intense laser pulse is considered.

The electromagnetic wave is propagating along the \vec{e}_z axis, with a wave vector $\vec{k}_i = 2\pi/\lambda_L \vec{e}_z$ and a frequency $\omega_i = 2\pi c/\lambda_L$ and with a normalized vector potential given by:

$$\vec{a} = a_0 \left[\frac{1}{\sqrt{2}} \cos(\omega_i t - k_i z) \vec{e}_x + \frac{1}{\sqrt{2}} \sin(\omega_i t - k_i z) \vec{e}_y \right]$$

The equation of motion of the test electron is given by:

$$\frac{d\vec{p}}{dt} = -e(\vec{E} + \vec{v} \times \vec{B})$$

The Hamiltonian describing the test electron dynamics in the electromagnetic wave is:

$$\hat{H}(\hat{r}, \hat{p}, \hat{t}) = \gamma = \sqrt{1 + \hat{p}^2} = \sqrt{1 + (\hat{P} + \vec{a})^2}$$

All quantities with a hat are normalized by the choice of units: $m = c = e = \omega_i = 1$

According to the Noether theorem, it is possible to analyze the symmetries of the system to find the conserved quantities. The Hamiltonian \hat{H} depends on the canonical momentum \hat{P} and on the potential vector $\vec{a}(\varphi)$ through the variable $\varphi = \hat{t} - \hat{z}$. Hence \hat{H} is independent of \hat{x} and \hat{y} , which implies that the transverse canonical momentum is a constant of motion. In addition \hat{H} depends on \hat{t} and \hat{z} only through $\varphi = \hat{t} - \hat{z}$. Thus, $\partial \hat{H} / \partial \hat{t} = -\partial \hat{H} / \partial \hat{z}$ which leads to the second constant of motion C:

$$\gamma - \hat{p}_z = C$$

At the initial condition (electron at rest) $C=1$, because if the electron is at rest $\gamma = 1$ and $\hat{p}_z = 0$.

The test electron orbit is obtained by integrating the constants of motion:

$$\hat{x}(\varphi) = \frac{a_0}{\sqrt{2}} \sin(\varphi);$$

$$\hat{y}(\varphi) = -\frac{a_0}{\sqrt{2}} \cos(\varphi);$$

$$\hat{z}(\varphi) = \frac{a_0^2}{4} \varphi;$$

$$\gamma = 1 + \frac{a_0^2}{4};$$

The electron motion in the laser field consists of a drift in the longitudinal direction combined with a transverse oscillation. The normalized energy γ is constant. The trajectory takes place in three dimensions and is helical. In the nonlinear case ($a_0 \gg 1$), the electron generates

smaller wavelength radiation than the incident laser pulse. The period of the electron motion is given by:

$$\lambda_u = \frac{a_0^2}{4} \lambda_L$$

Radiation properties

For $a_0 > 1$, the relativistic electron motion described above leads to the emission of nonlinear Thomson scattering radiation whose features can be calculated with the general formalism of the radiation emitted from a moving charge. The motion is driven in the wiggler regime since the nonlinear case $a_0 > 1$ is considered. The spectrum is broadband and extends up to the critical energy:

$$\hbar\omega_c = \frac{3}{2} \gamma^3 \hbar \frac{c}{\rho}$$

where $\rho \equiv (\lambda_L / 2\pi) \cdot \sqrt{2} a_0^3 / 16$ is the instantaneous radius of curvature of the electron orbit obtained from the trajectory. Basically, the critical energy grows as a_0^3 for $a_0 \gg 1$. In practical units, it reads:

$$\hbar\omega_c [eV] = 0.3 \frac{a_0^3}{\lambda_L [\mu m]}$$

Radiation is emitted in the direction of the electron velocity and has the same symmetry as the electron orbit. For circular polarization, the radiation is emitted symmetrically around the laser propagation axis at an angle $\vartheta \equiv 2\sqrt{2}/a_0$, within a typical angular width $\Delta\vartheta = 1/\gamma \equiv 4/a_0^2$. The number of photons emitted at the mean energy $\langle \hbar\omega \rangle = 0,3\hbar\omega_c$ per one electron undergoing one oscillation period, in practical units is:

$$N_\gamma = 4.68 \cdot 10^{-2} a_0 \quad \text{for} \quad a_0 \gg 1.$$

Numerical results

In this section, the case of a linearly polarized laser field is studied using numerical simulations. Electron orbits and radiation features are presented. Here is not possible to apply the concept of wiggling seen before. The laser pulse duration (FWHM) is $\tau=20$ fm and the polarization is linear along the \vec{e}_x direction. The test electron is initially at rest.

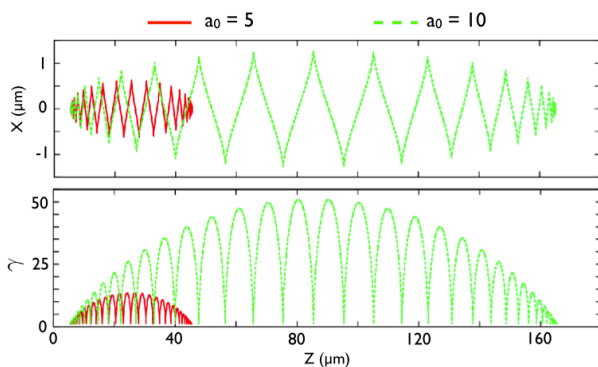


Fig. 5.2.

Top: Electron orbit in an intense linearly polarized laser pulse $a_0 = 5$ (red line) and $a_0 = 10$ (green line).

Bottom: The γ factor as a function of the longitudinal position for each case.

Reproduced from Corde et al. (2013).

Figure 5.2. shows the electron orbit for $a_0 = 5$ and $a_0 = 10$ and the evolution of the relativistic factor of the electron (γ) along its motion. The trajectory consists of successive straight lines with violent longitudinal acceleration or deceleration, the velocity vanishes at each corner. The electron acquires energy in the tens of MeV range while oscillating in the laser pulse, and is again at rest once the laser has passed. The radiation emitted has been calculated using the general formula (1).

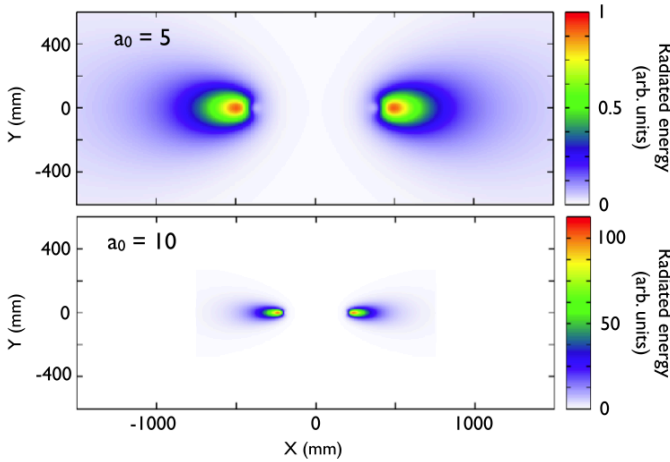


Fig. 5.3.

Spatial distribution of the nonlinear Thomson scattering corresponding to the trajectories of figure 5.2. This figure represents the radiated energy per unit surface in the plane situated at 1 m from the source and perpendicular to the propagation axis.

Reproduced from Corde et al. (2013).

Figure 5.3 shows the spatial distribution of the radiated energy. Because the polarization is linear, the radiation consists of two lobes corresponding to the two directions pointed by the straight lines of the orbit. These two lobes form an angle ~ 450 mrad for $a_0 = 5$ and ~ 230 mrad for $a_0 = 10$. As expected, the radiation is more collimated for stronger a_0 . An estimate of the total photon number can be obtained assuming that all electrons in the focal volume participate to the emission. For example, assuming a focal volume of $10 \times 10 \times 1000 \mu\text{m}^3$ and a density of 10^{18} cm^{-3} gives 10^{11} electrons, which radiate $\sim 10^7$ photons/(0.1%BW/shot) for $a_0 = 5$ and $\sim 1.5 \cdot 10^7$ photons/(0.1%BW/shot) for $a_0 = 10$. The shape of the spectrum is not synchrotron-like because, for a linearly polarized laser, the electron orbit does not correspond to a wiggling motion. The radiation for linear polarization is due to the longitudinal acceleration from $\gamma = 1$ to $\gamma = 1 + a_0^2/2$ and deceleration to $\gamma = 1$ occurring for for each straight-line section of the trajectory. The time profile of the emitted radiation in a single straight-line section consists of a double peak structure: the first corresponds to the moment when the acceleration is maximal and the second to the moment when the deceleration is maximal. Scattered photons should be radiated at harmonics of the frequency of the incident laser light, with each harmonic having its own unique angular distribution.

In conclusion, three main properties characterize the nonlinear Thomson scattering radiation: first, the x-ray intensity increases linearly with the number of electron oscillating inside the laser field (indicative of the incoherent process); second, the x-ray spectrum is broadband and peaked; third, the emission is strongly anisotropic.

Experimental results

Nonlinear Thomson scattering was observed for the first time in 1998 at the Center for Ultrafast Optical Science in USA (Chen, Maksimchuk, and Umstadter, 1998) using a 4 TW laser pulse with a duration of 400 fs, $\lambda_L = 1.053 \mu\text{m}$ and $a_0 \cong 2$. The laser beam, 50 mm in diameter, was focused onto the front edge of a supersonic helium gas jet. The focal spot consisted of a Gaussian spot with FWHM of $7 \mu\text{m}$ (containing the 60% of the total energy). The measured radiation followed the specific features of nonlinear Thomson scattering. In particular, the

spatial distribution measured was consistent with the nonlinear Thomson scattering properties obtained from the numerical simulation. In this experiment, radiation was detected up to the third harmonic of the laser.

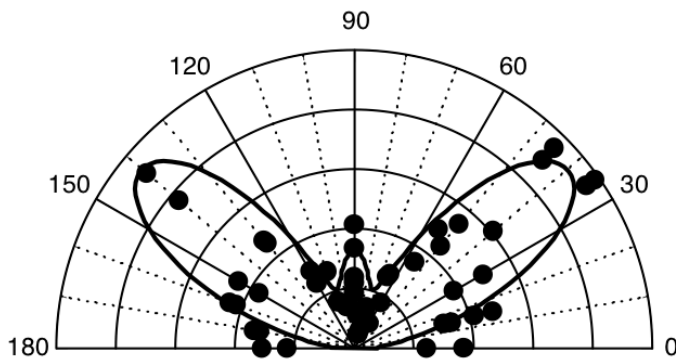


Fig. 5.4.
Angular pattern of the third-harmonic light.
Reproduced from Chen, Maksimchuk, and Umstadter (1998)

Figure 5.4 shows a polar plot of the intensity (in arbitrary units) of the third harmonic light as a function of azimuthal angle (in degrees). Filled circles represent experimental data. The solid line represents the theoretical results.

In 2003, thanks to the advent of high-intensity lasers, nonlinear Thomson scattering was demonstrated in the XUV range (Ta Phuoc et al., 2003; Ta Phuoc, Rouse et al., 2003; Ta Phuoc, Burgy, Rousseau and Rouse, 2005). The experiment was conducted at the Laboratoire d'Optique Appliquée (Palaiseau, France) using a 50 TW laser with $a_0 = 5.6$, 30 fs laser pulse, 800 nm wavelength and a helium gas. The experimental setup is shown in figure 5.5.

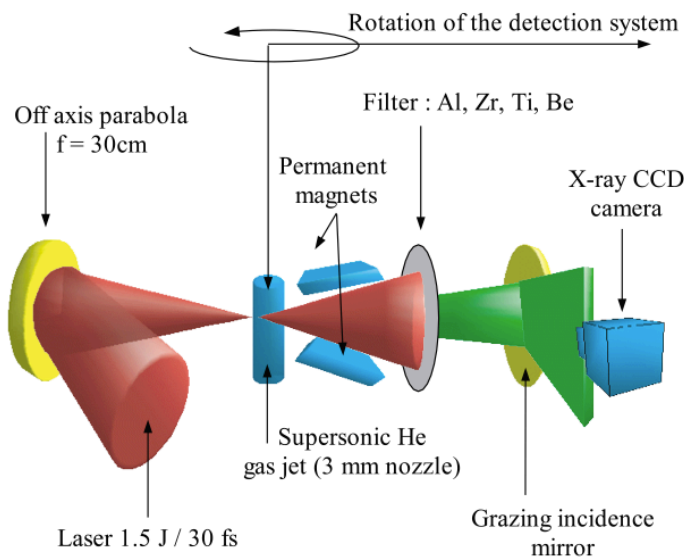


Fig. 5.5.
Experimental setup.
Reproduced from Ta Phuoc, Rouse et al. (2003)

The laser beam, 55 mm in diameter, was focused within a parabolic mirror onto the front edge of a supersonic gas jet (3 mm in diameter). Electron densities from 10^{18} to 10^{19} cm⁻³ were used in the experiment. The diameter of the focal spot was 6 μ m (FWHM) and contained 60% of the laser energy. The laser strength parameter was $a_0 = 5.6$ for linear polarization. The radiation was collected with grazing incidence metallic mirror (nickel or gold) and focused into an x-ray charge-coupled device (CCD) camera. Filters were positioned between the plasma and the detector to block the laser infrared light. A static magnetic field (0.5 T) was inserted between the plasma and the x-ray spectrometer to deviate the electrons accelerated in the forward direction out of the detector. The angular dependency of the x-ray

emission was obtained by rotating the entire spectrometer around the laser focal spot. The experimental results are presented in figure 5.6.

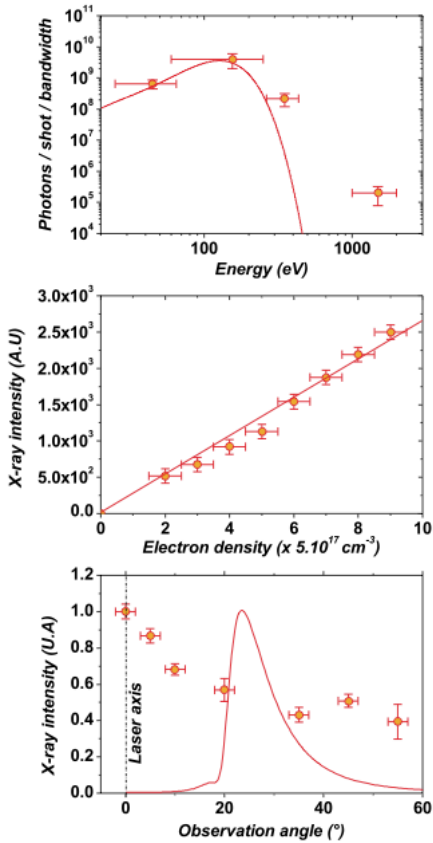


Fig. 5.6.

a) Energy spectrum of the observed x-ray emission. The horizontal bars correspond to each spectral bandwidth of the x-ray spectrometer. The vertical error bars correspond to the statistical uncertainty accumulated over five shots.

b) X-ray intensity as a function of the electron density on the plasma.

c) Angular distribution of the emitted radiation.

Solid curves: numerical results of the free electron model.

Reproduced from Ta Phuoc, Rousse et al. (2003)

The observed x-ray signal is found to increase linearly with the electron density, to be broadband and peaked at 150 eV, to be anisotropic. Such features are consistent with the expected three unique properties of the nonlinear Thomson scattering radiation mentioned previously. However the results differ from the expected emission. The spatial distribution of the radiation, presented in figure 5.6(c), was collimated within a large angle and was maximum on axis instead of consisting in two lobes centred at $+23^\circ$ and -23° with an opening angle of 10° . The simplest model of a free electron initially at rest (in a plane electromagnetic wave) appears to be insufficient to describe the electron-photon interaction. Additional effects such as plasma-accelerated electrons must be taken into account and results in a shift and a broadening of the characteristic angle of emission. Numerical simulations were done to estimate this effect on the spatial distribution. In these simulations, mono-energetic electrons at 0.7 MeV produce an emission centred on $\theta=10^\circ$ instead of 23° for free electrons; mono-energetic electrons at 1.6 MeV produce a further collimate radiation centred on $\theta=4^\circ$. The best fit of the experimental data is shown in figure 5.7.

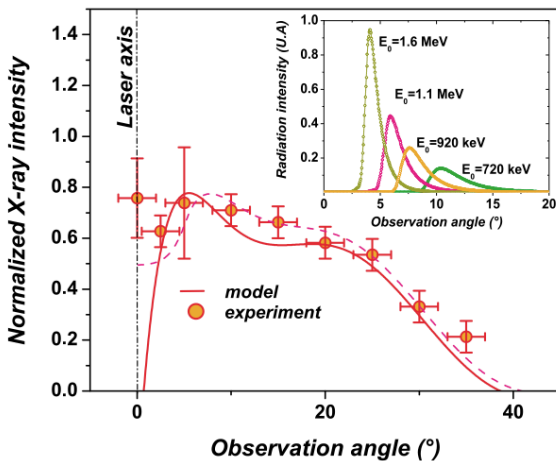


Fig. 5.7.

Spatial distribution of the observed x-ray. The solid line (dotted line) is the numerical result obtained for a Gaussian electron distribution with an energy of 0.9 MeV and without (with) 5° \vec{k} spread (which can come from either the divergence of the electron beam or the spread of the k vector of the laser).

Reproduced from Ta Phuoc, Rousse et al. (2003)

B) Thomson backscattering

X-ray or gamma-ray can be produced by scattering an electromagnetic wave off a counter-propagating relativistic electron bunch. This scheme was first proposed in 1963 (Arutyunian and Tumanian, 1963; Milburn, 1963) and reinvestigated during 1990s thanks to the advance in laser technology and electron accelerators. More recently, it was proposed to use laser-plasma accelerated electron bunches to develop an all-optically driven scheme (Catravas, Esarey and Leemans, 2001; Hafz et al., 2003; Leemans et al., 2005; Tomassini et al., 2005; Hartemann et al., 2007). Figure 5.8 shows the principle of this scheme.

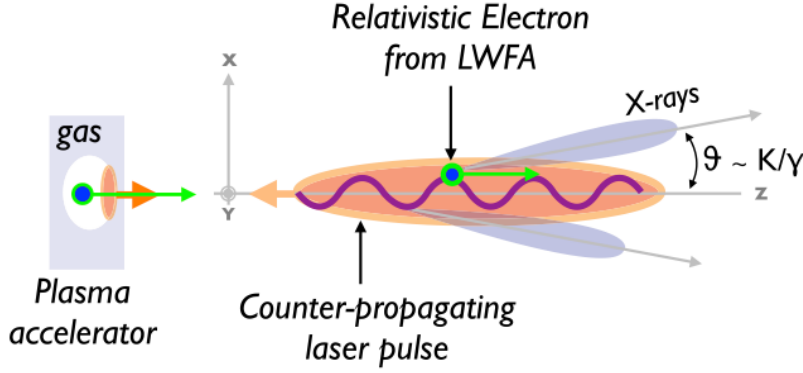


Fig. 5.8. Scheme of the all-optically driven Thomson backscattering source. Reproduced from Corde et al. (2013).

Two laser pulses are required: the first drives the plasma accelerator, as discussed in section 2, and the second (counter-propagating laser) scatters off the accelerated electrons.

Electron motion

A laser-plasma accelerator producing a mono-energetic electron bunch of energy $E = \gamma_i m c^2$ with a velocity directed along \vec{e}_z , is considered. The counter-propagating laser pulse is represented by a linearly polarized plane electromagnetic wave of wave vector $\vec{k}_i = -2\pi/\lambda_L \vec{e}_z$ and frequency $\omega_i = 2\pi c/\lambda_L$, and with a normalized vector potential give by $\vec{a} = a_0 \cos(\omega_i t + k_i z) \vec{e}_x$. The equation of motion is given by:

$$\frac{d\vec{p}}{dt} = -e(\vec{E} + \vec{v} \times \vec{B})$$

The Hamiltonian describing the test electron dynamics in the electromagnetic wave is:

$$\hat{H}(\hat{r}, \hat{p}, \hat{t}) = \gamma = \sqrt{1 + \hat{p}^2} = \sqrt{1 + (\hat{P} + \vec{a})^2}$$

All quantities with a hat are normalized by the choice of units: $m = c = e = \omega_i = 1$.

According to the Noether theorem, it is possible to analyze the symmetries of the system to find the conserved quantities. The Hamiltonian \hat{H} depends on the canonical momentum \hat{P} and on the potential vector $\vec{a}(\varphi)$ through the variable $\varphi = \hat{t} - \hat{z}$. Hence \hat{H} is independent of \hat{x} and \hat{y} , which implies that the transverse canonical momentum is a constant of motion. In addition \hat{H} depends on \hat{t} and \hat{z} only through $\varphi = \hat{t} - \hat{z}$. Thus, $\partial \hat{H} / \partial \hat{t} = -\partial \hat{H} / \partial \hat{z}$ which leads to the second constant of motion C:

$$\gamma - \hat{p}_z = C$$

The constant C is obtained using the initial conditions $\gamma = \gamma_i$, $\hat{p}_z = \sqrt{\gamma_i^2 - 1}$. The integration of the constants of motion gives the electron orbit.

$$\hat{x}(\varphi) = \frac{a_0}{C} \sin(\varphi);$$

$$\hat{y}(\varphi) = 0;$$

$$\hat{z}(\varphi) = \left\{ \frac{1}{2} - \frac{1 + a_0^2/2}{2C^2} \right\} \varphi - \frac{a_0^2}{8C} \sin(2\varphi);$$

$$\gamma = \frac{C}{2} + \frac{1 + a_0^2 \cos^2(\varphi)}{2C};$$

$$\text{where } C = \gamma_i + \sqrt{\gamma_i^2 - 1}.$$

The trajectory obtained doesn't exactly correspond to the standard sinusoidal trajectory studied in section 2. Here γ is not constant along the orbit. The oscillation motion z takes, however, a form similar to the sinusoidal trajectory. The description of section 2 can be recovered with the approximation $\varphi \cong 2\hat{z} \cong 2\hat{t}$. The counter-propagating laser pulse can be seen as an undulator with a spatial period given by: $\lambda_u = \lambda_L / 2$.

The strength parameter is given by: $K = a_0 = 0.855 \sqrt{I [10^{18} \text{ W/cm}^2] \lambda_L^2 [\mu\text{m}]}$.

Radiation properties

The qualitative features of the radiation remain the same as in section 2. The spectrum of the emitted radiation depends on the amplitude of the parameter K. For $K \ll 1$, the electromagnetic wave acts as an undulator. In the average rest frame of the electron, Thomson scattering occurs in the linear regime. As $K \rightarrow 1$, harmonics of the fundamental start to appear. For $K \gg 1$, the electromagnetic wave acts as a wiggler, and the spectrum contains harmonics up to a critical energy $\hbar\omega_c$. A nonlinear Thomson scattering occurs in the average rest frame of the electron. These energies are, in practical units, given by:

$$\hbar\omega [eV] = 4.96\gamma^2 / \lambda_L [\mu\text{m}] \quad \text{for } K \ll 1$$

$$\hbar\omega_c [eV] = 3.18\gamma^2 \sqrt{I [10^{18} \text{ W/cm}^2]} \quad \text{for } K \gg 1$$

The radiation is collimated within a cone of typical opening angle $1/\gamma$ in the undulator case. For a wiggler, the radiation is collimated within a typical opening angle K/γ in the electron motion plane and $1/\gamma$ in the orthogonal plane. It is found that the duration of the electron bunch is femtoseconds (Lundh et al., 2011), so the duration of the x-ray pulse is femtoseconds as well. The number of emitted photons per period and per electron, in practical units, is given by:

$$N_\gamma = 1.53 \cdot 10^{-2} K^2 \quad \text{for } K \ll 1$$

$$N_\gamma = 3.31 \cdot 10^{-2} K \quad \text{for } K \gg 1$$

Numerical results

The electron equation of motion can be numerically integrated. The case of an electron initially propagating in the \vec{e}_z direction with $\gamma=200$ is considered. The wavelength of the counter-propagating laser is $\lambda_L = 0.8\mu\text{m}$ and two laser strength parameters are considered: $a_0 = 0.2$ for the undulator case and $a_0 = 2$ for the wiggler case. Figure 5.9 shows the orbit of a test electron travelling in the counter-propagating laser pulse for each situation.

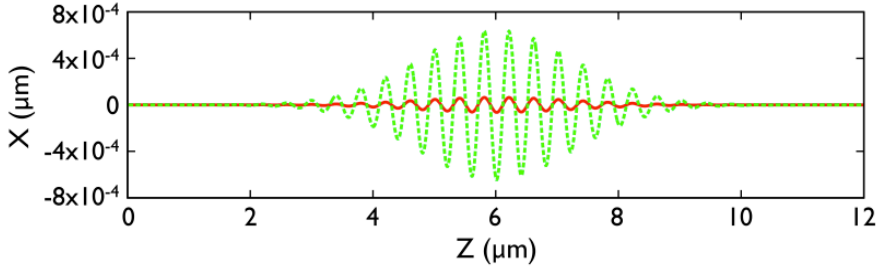


Fig. 5.9. Electron trajectories. The red line represents the undulator case. The green line represents the wiggler case. *Reproduced from Corde et al. (2013).*

The transverse motion consists of an oscillation at a period of $\lambda_u = \lambda_L/2 = 0.4\mu\text{m}$ and its amplitude increases as a_0 increases. The maximum amplitudes are $6.4 \cdot 10^{-5}\mu\text{m}$ and $6.4 \cdot 10^{-4}\mu\text{m}$ for $a_0 = 0.2$ and $a_0 = 2$ respectively. The left part of figure 5.10 shows the spatial distribution of the radiation produced by the electron along these trajectories.

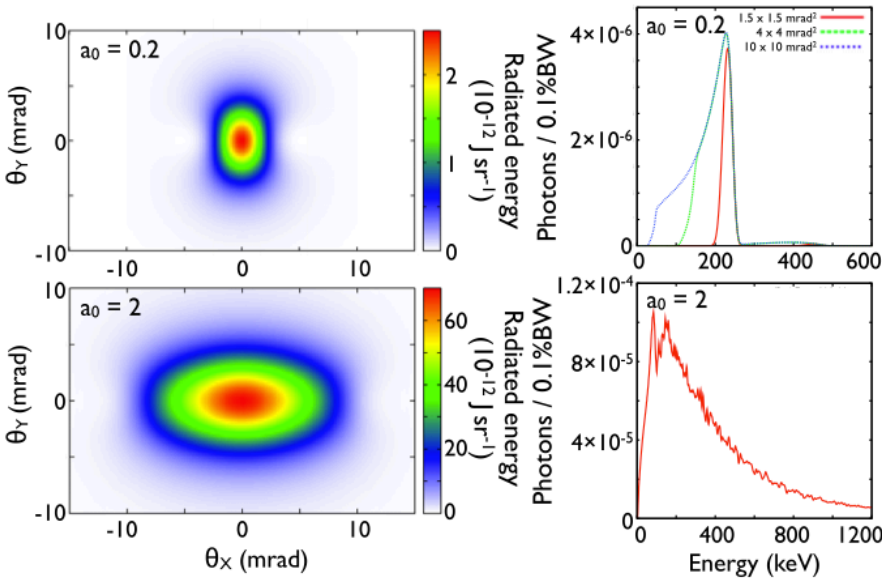


Fig. 5.10. On the left are represented the angular distributions of the radiation. On the right are shown the corresponding spectra. The undulator case is on the top. The wiggler case is on the bottom. *Reproduced from Corde et al. (2013).*

For $a_0 = 0.2$ (top), the radiation has a divergence of typical opening angle $1/\gamma \sim 5$ mrad. For $a_0 = 2$ (bottom), the radiation has a divergence of typical opening angle $a_0/\gamma \sim 10$ mrad in the plane of the electron motion and $1/\gamma \sim 5$ mrad in the orthogonal direction. The right part of figure 5.10 shows the spectra of the emitted radiation, integrated over three selected solid angles for the undulator case, and over the overall angular distribution for the wiggler case. In the undulator case, the spectrum is nearly monochromatic at the energy of $\hbar\omega \sim 200$ keV in the forward direction, and it is broadened after integration over the emission angles due to the angular dependence of the radiated wavelength: $\lambda \cong (\lambda_u/2\gamma^2)(1 + K^2/2 + \gamma^2\theta^2)$. In the wiggler case the spectrum becomes broadband with a critical energy of about 300 keV. In the wiggler case, a total photon number in the range $10^7 - 10^8$ is expected.

Experimental results

Many experiments of Thomson backscattering have been performed using electrons from conventional accelerators. The first one was conducted at SLAC (in USA) in 1969 (Ballam et al., 1969). A significant experiment has been performed by Schoenlein and co-workers (Schoenlein et al., 1996; Leemans et al., 1997) at Jena University (in Germany). They demonstrate femtosecond x-ray generation using Thomson backscattering with electrons from a conventional accelerator. In 2006, Schwoerer (Schwoerer et al., 2006) performed the first experiment of production of Thomson backscattering radiation using an all-optically driven scheme. This experiment was based on the use of two laser pulses in a counter-propagating geometry. Figure 5.11 shows the experimental setup.

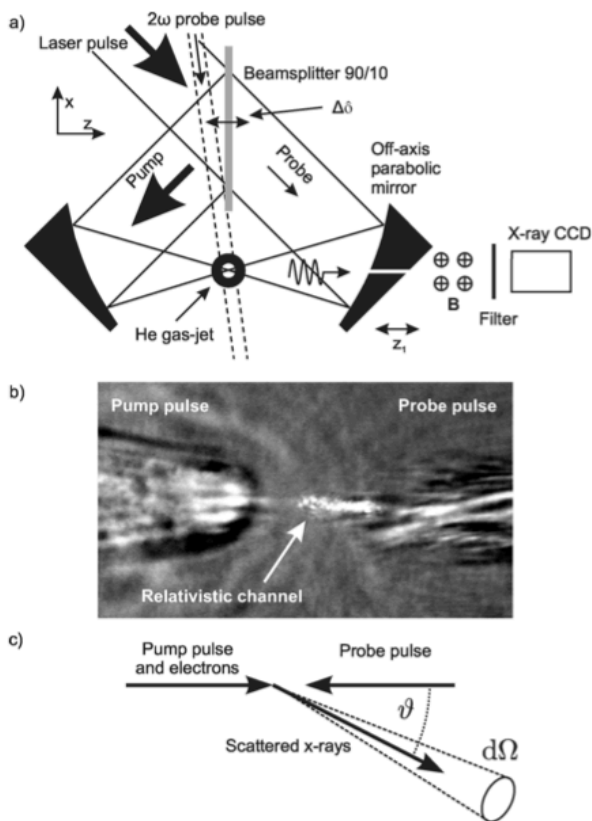


Fig. 5.11.

a) Setup of the Experiment. The main laser pulse is divided into two pulses, by a 90/10 beam splitter, both of which are focused by off-axis parabolic mirrors into an Helium gas jet. The radiation is observed using a CCD camera. A frequency-doubled laser pulse is used for shadowgraphy of the interaction region.

b) Shadowgram of the interaction region.

c) Interaction scheme: θ is the angle of observation with respect to the electron propagation, and $d\Omega$ is the solid angle of detection.

Reproduced from Schwoerer et al., 2006.

The ultrashort laser pulse is divided by a 90/10 beam splitter into a pump pulse and a probe pulse. Each of the pulses is focused by an off-axis parabolic mirror into a He gas jet. The pump pulse (85 fs, 800 nm, and $a_0 = 3$) was used to produce an electron bunch. The probe pulse (85 fs, 800 nm, and $a_0 = 0.8$) was counter-propagating and focused on the electron bunch. The time delay between the laser pulses may be adjusted by moving the beam splitter as indicated in figure 5.11. The setup is located in a vacuum chamber and computer controlled. The probe pulse is scattered from accelerated high-energy electrons, and the backscattered x-ray photons are observed. A hole of 3 mm diameter was drilled into the parabolic mirror of the probe beam, aligned with the axis of the electron beams. An x-ray CCD camera operating in single-photon counting mode was placed on this axis. A 30 nm nickel filter was introduced before the x-ray CCD to block irradiation by laser light. A pair of cylindrical dipole magnets was used to prevent electrons from reaching the x-ray CCD chip. In this experiment about $3 \cdot 10^4$ x-ray photons in the 400 eV – 2 keV range were observed within a $80 \mu\text{sr}$ detection cone at 60 mrad with respect to the laser axis. However, this type of experiment remains challenging because of the difficulty to overlap in time and space the electron bunch and the

counter-propagating laser pulse. Recently, a much simpler and efficient method, based on the use of one laser pulse only, has been demonstrated (Ta Phuoc et al. 2012) at the Laboratoire d'Optique Appliquée (in France). This technique will lead to a compact source of femtosecond, tunable and low-divergence photons. As shown in figure 5.12, an intense femtosecond laser pulse focused into a millimetre-scale gas jet drives a wakefield cavity in which electrons are trapped and accelerated. A foil is positioned close to the exit of the gas jet and at nearly normal incidence with respect to the laser and electron beam axis \hat{z} . The foil is ionized by the rising edge of the laser pulse, resulting in a plasma mirror that efficiently reflects the laser pulse (the reflectivity is expected to be larger than 70% for $a_0 \geq 0.04$). This approach provides an inherent overlap in time and space of the back-reflected laser pulse and the relativistic electron bunch, that starts to oscillate in the laser field and emits a bright femtosecond x-ray beam by Thomson backscattering. Figure 5.12 (b) shows the experimental setup.

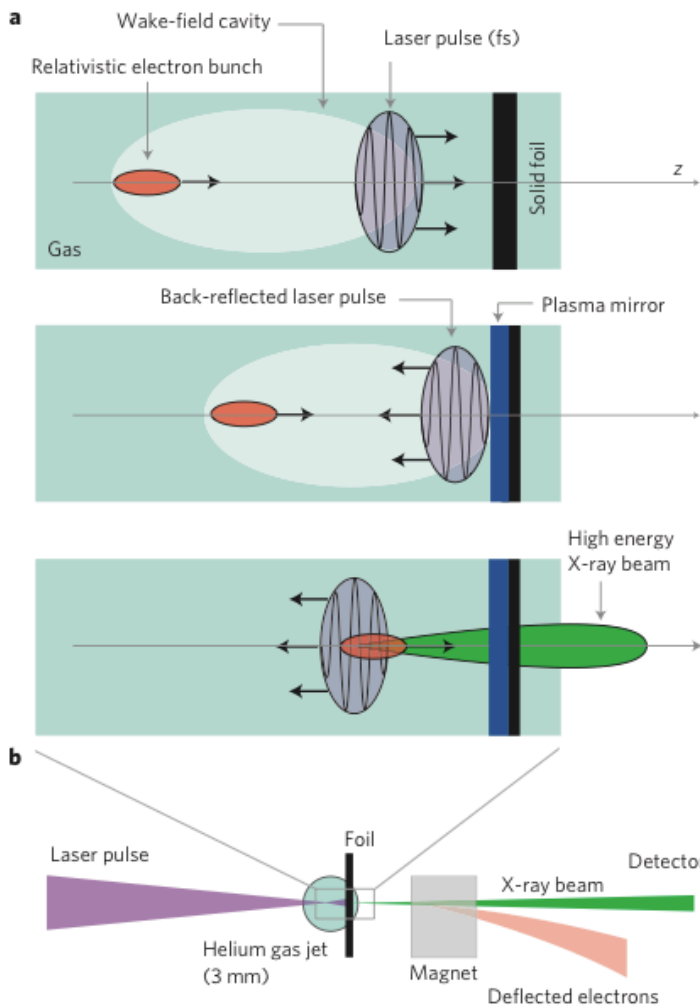


Fig. 5.12.
a) Principle of the Thomson backscattering using only one laser pulse and a plasma mirror.
b) Experimental setup.
Reproduced from Ta Phuoc et al., 2012.

The relativistic laser pulse (30 TW) is focused into a 3 mm Helium gas jet to produce an electron beam. The measured charge in an electron bunch was ~ 120 pC. In this relativistic interaction, radiative process other than Thomson backscattering can produce x-ray radiation. Careful measurements were performed to identify, evaluate and minimize their contribution to the overall emission. In our parameter regime, betatron radiation is emitted in the few keV range and $\sim 10^8 - 10^9$ photons are produced. This radiation was measured and blocked by filters (glass and aluminium). Relativistic Bremsstrahlung radiation can be produced when the electron bunch crosses the foil. Bremsstrahlung radiation is dependent on the material and thickness of the foil and was minimized by using a thin low-Z foil for the

plasma mirror. Figure 5.13 shows the spectrum of the Thomson backscattering radiation measured using a set of copper (Cu) and aluminium (Al) filters and shows the angular profile measured using a phosphor screen.

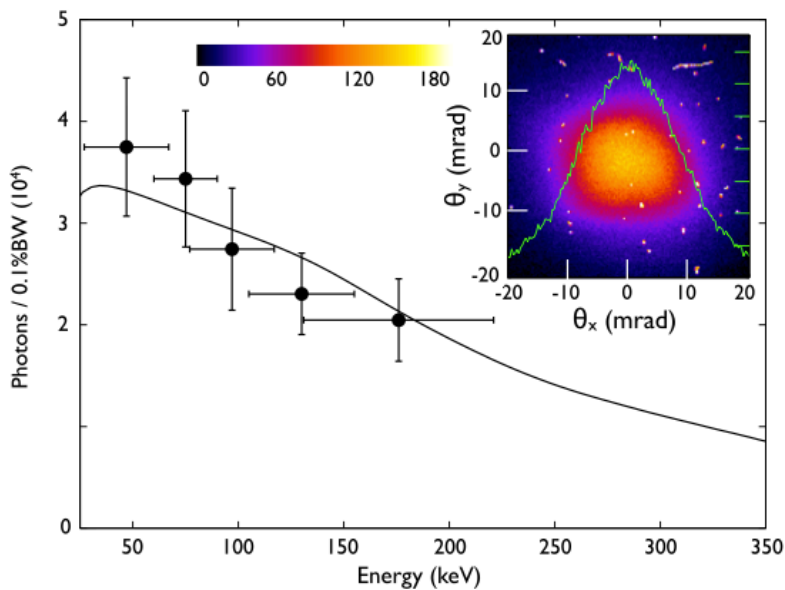


Fig. 5.13. Spectrum and angular profile of the Thomson backscattering radiation. *Reproduced from Corde et al. (2013).*

The spectrum extends, as expected, up to a few hundreds of keV and the total photon number is $\sim 10^8$. The radiation is collimated within a cone of divergence 18 mrad (FWHM). Finally, the source size was estimated to be less than $3 \mu\text{m}$. Such energetic radiation can be used to image the interior of a thick or dense object. For example, figure 5.14 presents a radiograph of a USB flash drive obtained with this source.

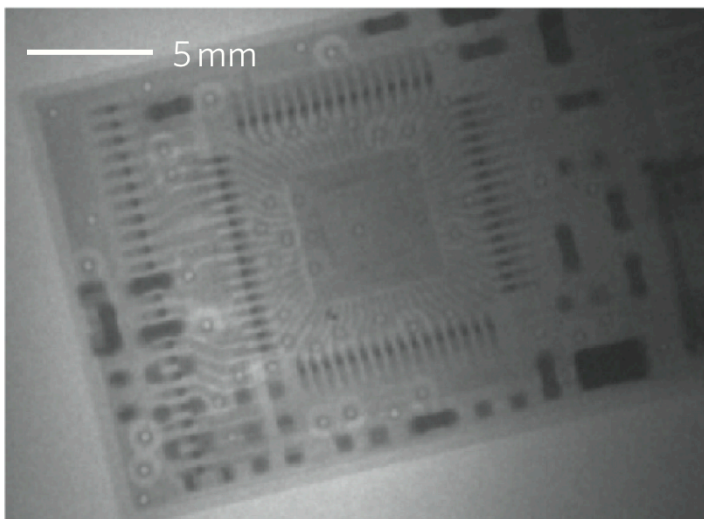


Fig. 5.14 Radiograph of a USB flash drive. *Reproduced from Ta Phuoc et al., 2012.*

This source is 10000 brighter than Thomson x-ray sources from conventional accelerators (Schoenlein et al., 1996; Albert et al., 2010). This high brightness is obtained thanks to the micron source size and the femtosecond duration reached in this all-optical scheme.

06. The Free Electron Laser (FEL)

The free electron laser concept was first proposed by Madey in 1971. He realized that a laser-like amplifier could be constructed by combining a high quality electron beam with an undulator or a wiggler and an input radiation beam. A few years later the principle was demonstrated experimentally by Madey and co-workers (Deacon et al., 1977). In practice, injecting an electron beam in an undulator, will naturally lead to incoherent synchrotron emission, as discussed in the previous sections. This incoherent emission provides the input radiation beam and can be amplified by the FEL process when certain conditions are met (Kondratenko and Saldin, 1980; Bonifacio, Pellegrini and Narducci, 1984; Murphy and Pellegrini, 1985; Bonifacio et al., 1994; Saldin, Schneidmiller and Yurkov, 1998). Figure 6.1 shows the mechanism of the free electron laser amplification.

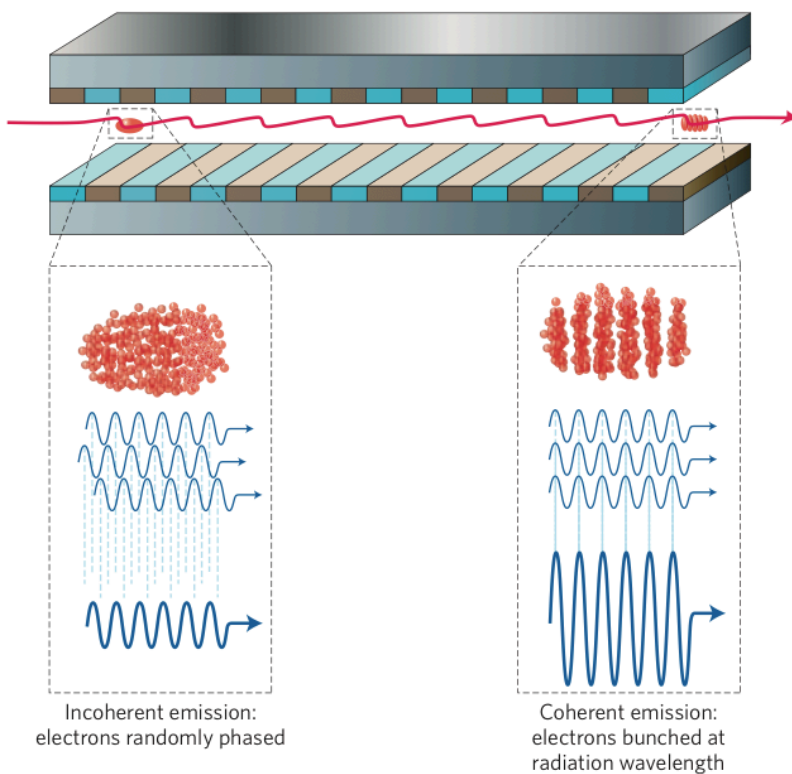


Fig. 6.1.

FEL operating principle.

When electrons enter the undulator, their initially random phases cause a mostly incoherent radiation emission at the resonant radiation wavelength (left). Then, electrons start to interact with the radiation they emit, small coherent fluctuations in the radiation field grow and simultaneously begin to bunch the electrons at the resonant wavelength.

Reproduced from McNeil and Thompson (2010).

A single electron experiences the radiation from other electrons in the bunch. This interaction between the bunch and its own radiation can lead to a micro-bunching of the electron distribution. This micro-bunching in return leads to coherent emission from the overall electron bunch, whose power is order of magnitude higher than usual incoherent synchrotron radiation. However, this free electron laser mechanism requires restrictive conditions. This situation, in which the incoherent synchrotron or spontaneous emission is amplified in a single pass, is commonly named Self-Amplified Spontaneous Emission (SASE) configuration, and brings a fluctuating radiation output with poor temporal coherence. The SASE configuration seems to be the simplest way to produce hard x-ray radiation. It is worth to notice that the electron beam is accelerated using the laser-plasma interaction and the undulator can be a conventional undulator, an electromagnetic wave undulator or a plasma undulator.

Principle of the FEL process

To understand the physical mechanism of the FEL amplification, the interaction of a single electron with the radiation beam and the undulator is considered (Braun, 1990a; Saldin, Schneidmiller and Yurkov, 2000; Huang and Kim, 2007). In the following, a conventional undulator is considered, in order to present the FEL amplification process and the required conditions on the electron beam parameters. The undulator forces the electron to follow a sinusoidal trajectory whose period corresponds to the undulator period λ_u and whose amplitude is $K\lambda_u/(2\pi\gamma)$, where the term K is the undulator strength parameter. The electron propagates in the z direction and the magnetic field is in the y direction. The motion of the electron is in the x - z plane. In terms of velocity, the electron motion inside the undulator is written as:

$$\beta_x(z) = \frac{K}{\gamma} \cos(k_u z)$$

where $k_u = 2\pi/\lambda_u$, $\vec{\beta}_x = \vec{\beta} \cdot \vec{e}_x$ and $\vec{\beta} = \vec{v}/c$ is the electron velocity normalized to the speed of light. The radiation beam is modelled by a linearly polarized plane electromagnetic wave, whose electric field is $\vec{E} = E_0 \sin(kz - \omega t) \vec{e}_x$ where $\omega = 2\pi c/\lambda$ is the frequency. Using the kinetic energy theorem and assuming that the radiation field is small compared to the undulator field, the rate of electron energy change is:

$$\frac{d\varepsilon}{dz} \equiv \frac{d\varepsilon}{cdt} = -e\vec{\beta} \cdot \vec{E} = -\frac{eKE_0}{\gamma} \cos(k_u z) \sin(kz - \omega t) = -\frac{eKE_0}{2\gamma} [\sin\psi + \sin(kz - \omega t - k_u z)]$$

where $\psi = kz - \omega t + k_u z$ is the ponderomotive phase. This formula shows that an energy exchange between the electron and the radiation is possible. In case of several electrons interacting with the radiation, half of them lose energy, while the other half gain energy. This process causes the electrons to bunch at the radiation wavelength, allowing a coherent interaction between the electrons and the radiation. As shown in figure 6.2, the forces that bunch the electrons can be considered as a series of periodic potential wells travelling at the resonant electron velocity, which is referred to as a ‘‘ponderomotive’’ potential.

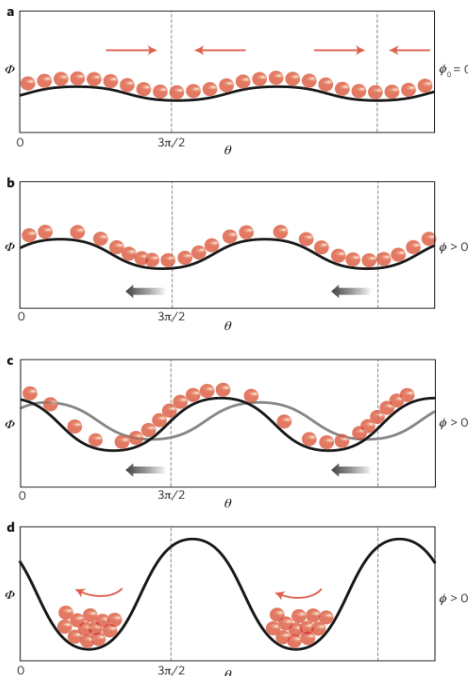


Fig. 6.2.

The interaction between electrons and radiation.

A small radiation field of initial phase $\phi_0=0$ is applied to the electrons at the start of the undulator. ϕ represents two ponderomotive potential wells. The forces on the electrons (red arrows) tend to induce a small electron bunching about $\theta=3\pi/2$ and $\theta=7\pi/2$. This small bunching drives the radiation phase ϕ , shifting the wells to the left ($\theta+\phi$). The weakly bunched electrons begin to fall into the potential wells, losing kinetic energy to the radiation field and increasing the depth of the potential well. This radiation phase shifting, electron bunching and energy exchange from electrons to the field continues exponentially. The system saturates when the now strongly bunched electrons begin to re-absorb energy from the field.

Reproduced from McNeil and Thompson (2010).

The electromagnetic wave is always faster than the electrons. A resonant condition occurs, such that the radiation slips a distance λ relative to the electrons after one undulator period. It can be put in the following form:

$$\lambda = \frac{\lambda_u}{2\gamma^2}(1 + K^2/2) \quad (3)$$

This is the formula of the fundamental wavelength of the electromagnetic field radiated by the electron moving in the undulator. An energy exchange between the electrons and the radiation can occur if condition (3) is fulfilled. Thus, under certain favourable conditions, the interaction between the electron beam and the electromagnetic wave can be sustained, and a net transfer of energy from electron beam to photon beam occurs. The radiation generated by electrons, interacting back on the electron beam, induces a periodic modulation of the beam longitudinal density at the radiation wavelength λ (micro-bunching). A fraction of the radiation generated is coherent, so the radiation intensity is proportional to the square of the number of electrons. The density modulation leads to a higher radiation intensity that causes stronger density modulation. The result is an exponential growth in the radiation intensity as well as in the density modulation of the electron beam. The process eventually saturates at some maximum radiation output level. Figure 6.3 shows the radiation intensity growth as a function of the distance.

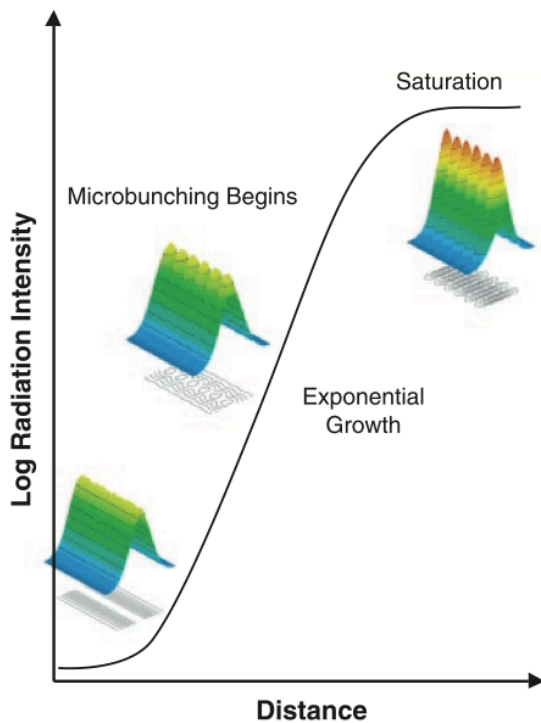


Fig. 6.3. Schematic representation of the longitudinal micro-bunching. The solid line represent the exponential growth of the optical signal as a function of distance along the undulator. Dark blue represents a low electron density; red represents a high electron density.
Reproduced from Milton et al., 2001

The amplification process can be summarized as follows:

- The electromagnetic radiation induces a modulation of the electron beam. The higher the electric field amplitude is, the faster the amplitude of the sinusoidal modulation grows.
- The electric field amplitude growth is proportional to the beam modulation. So, it results in an exponential amplification, $E_0 \propto \exp(z/2l_g)$ where $l_g^0 = \lambda_u/(4\pi\sqrt{3}\rho)$ is the gain length power (defined as the distance over which the power increases by a factor e and ρ is the Pierce parameter).

- The electron beam is micro-bunched at the radiation wavelength λ and radiates coherently. The largest fraction of output radiation is generated during this stage. This leads to a loss of energy for the electron beam and becomes off resonance. This corresponds to the saturation: the radiation energy cannot be increased further.
- Letting the process go on, electrons off-resonance can extract energy from the electromagnetic radiation, so they can satisfy again the resonance condition and they can amplify the radiation again. Hence, the radiation amplitude starts to oscillate after the saturation point.

Figure 6.4 shows the different stages of the process.

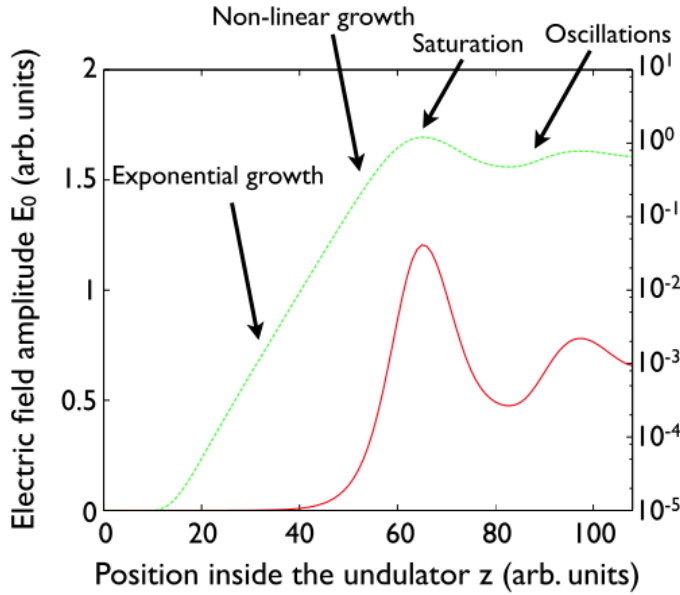


Fig. 6.4. Schematic of the FEL amplification process. Red line: linear scale (left y axis). Green line: logarithmic scale (right y axis). Reproduced from Corde et al. (2013).

The efficiency of the amplification process, defined as the ratio of the output total radiation energy to the total energy of the electron bunch, is limited at saturation. In the ideal one-dimensional case, the efficiency at the saturation equals the Pierce parameter ρ , which is small compared to unity in all cases. Looking at the formula (3) it is evident that a loss of electron energy (decreasing of γ) can be compensated by varying K , which allows the process to remain in resonance after the saturation point and to continue to radiate at the wavelength λ in a fully coherent manner. This approach permits to increase the efficiency (η) and even to approach the unit ($\eta \approx 1$). The Pierce parameter is defined as:

$$\rho = \left\{ \frac{I}{I_A} \frac{\gamma \lambda^2}{16\pi^2 \sigma_{tr}^2} \frac{K^2}{(1 + K^2/2)^2} \left[J_0\left(\frac{K^2}{4 + 2K^2}\right) - J_1\left(\frac{K^2}{4 + 2K^2}\right) \right]^2 \right\}^{1/3}$$

Where I is the peak current of the electron bunch, $I_A = 17.045$ A is the Alfvén current, J_0 and J_1 are Bessel functions, σ_{tr} is the electron bunch transverse root-means-square size. The pierce parameter is typically of the order of 0.001 for visible wavelength and shorter, so the gain length is of the order of 100 undulator periods. By including the effects of energy spread, angular divergence, the transverse beam size of the electron beam and also the diffraction of the electromagnetic wave, the gain length is increased by a factor $\chi > 1$; so $l_g = \chi l_g^0$; it is found empirically (K.-J. Kim and M. Xie, 1993) that the power at saturation is given by $P_s \approx 1.6 P_b / \chi^2$, where P_b is the kinetic power of the electron beam and it is found that the number of undulator periods required to reach the saturation is $N_s \approx \chi / \rho$.

In the steady-state 1D FEL theory, the Pierce parameter provides the following conditions applied on the electron beam and the output values of the main parameters:

- The root-mean-square relative energy spread of the electron beam has to be smaller than ρ ,

$$\frac{\Delta\varepsilon}{\varepsilon} \leq \rho$$

- The relative detuning of the mean energy ε_m of the electron beam from the resonance (ε_0 is the energy at resonance corresponding to a radiation wavelength λ) has to be smaller than ρ ,

$$\frac{\varepsilon_m - \varepsilon_0}{\varepsilon_0} \leq \rho$$

- The power gain length l_g is given by

$$l_g^0 = \frac{\lambda_u}{4\pi\sqrt{3\rho}}$$

- The efficiency of energy conversion from the electron beam to the radiation is given by

$$\eta \approx \rho$$

The undulator length providing the saturation depends on the energy of the input radiation. Its typical value is on the order of 20 gain lengths, $l_{sat} \approx 20l_g$. According to the above formulas, the Pierce parameter ρ has to be as higher as possible.

The spectral and temporal characteristics are more complicated. If there is a monochromatic coherent input radiation with wavelength λ (seed signal), then the monochromaticity will be preserved and the system acts as a coherent amplifier of the seed radiation. In the absence of an input seed signal, the incoherent spontaneous synchrotron radiation provides a seed for the FEL amplification process (SASE). The main advantage of this method is the possibility to extend FEL radiation to high-energy photons. However, because the input is a fluctuating quantity shot to shot, the quality of the output radiation is very low compared to the seeding case (in which the output inherits the quality of the external input). For the SASE case, the output power has very large fluctuations and very poor temporal coherence. The temporal profile and the spectrum are constituted of many spikes.

Experimental results

The first experimental demonstration was performed by Madey and co-workers (Deacon et al., 1977) at the High Energy Physics Laboratory in USA. Figure 6.5 shows a schematic diagram of the experimental setup.

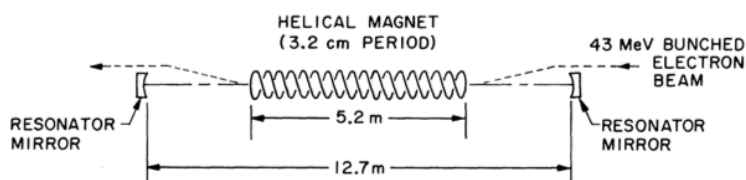


Figure 6.5. Schematic diagram of the free-electron laser oscillator. *Reproduced from Deacon et al. (1977).*

A superconductive helix generates a periodic transverse magnetic field. An electron bunch is fired along the axis of the helix. The radiation emitted by the electron beam is amplified and reflected by two mirrors at the ends of the interaction region. They demonstrated that the average power increases by a factor of 10^8 over the spontaneous radiation.

A major experiment demonstrating self-amplified spontaneous emission gain, exponential growth and saturation was performed by Milton et al., in 2001 at the Aragonne National Laboratory, in France. In the LEUTL (Low Energy Undulator Test Line) there are nine undulators installed along the path of the beam. The undulator period λ_u is 3.3 cm, and the peak on-axis field is 1 T, giving an undulator parameter K of 3.1. Each undulator is 2.4 m in length. Electron beam and optical diagnostics stations are located before the first undulator and after each undulator, for a total of 10 stations. The electron beam energy was 217 MeV, giving an output wavelength of 530 nm. The measured data are normalized to the intensity at the end of the first undulator. The spread is due to both the fluctuation of the SASE process and fluctuations in the beam properties entering the undulator. The saturation of the SASE process happened after the seventh undulator (16.8 m). The Full Width at Half Maximum (FWHM) bunch length is $\sim 140 \mu\text{m}$. The measure and simulated power gain curves for the beam parameters listed in the Table 1 are plotted in figure 6.5.

Parameter	A	B	C
Charge (nC)	0.30 ± 0.02	0.33 ± 0.007	0.30 ± 0.02
rms bunch length (ps)	0.19 ± 0.02	0.77 ± 0.05	0.65 ± 0.05
Peak current (A)	630 ± 78	171 ± 12	184 ± 19
Normalized emittance ($\pi \text{ mm} \cdot \text{mrad}$)	8.5 ± 0.9	8.5 ± 1.1	7.1 ± 0.5
rms energy spread (%)	0.4 ± 0.1	0.2 ± 0.1	0.1 ± 0.1
Nominal radiation wavelength (nm)	530	530	385
Measured gain length (m)	0.97	1.4	0.76
Calculated gain length (m)	1.0	1.3	0.80
Calculated FWHM angular divergence (mrad)	0.74	0.62	0.71
Measured FWHM angular divergence (mrad)	0.55 to 1.1	0.76 to 1.2	0.71 to 1.2

Table 1
Measured and calculated beam parameters.
Reproduced from Milton et al., 2001.

Column A shows data from 530 nm saturated conditions, column B shows data from 530 nm unsaturated conditions and column C shows data from 385 nm saturated conditions.

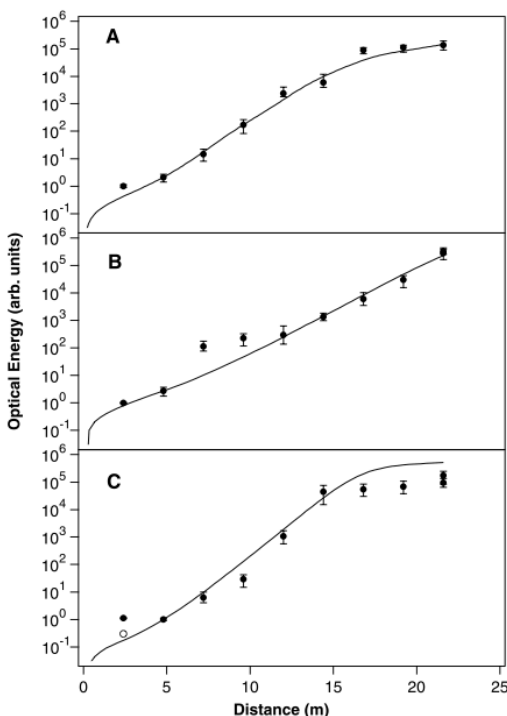


Figure 6.6.

Optical energy plotted as function of distance down the undulator, under various electron beam conditions. The solid curves represent simulation results using the beam parameters listed in Table 1. 100 images were taken at each diagnostic station and used to generate the data points.

Reproduced from Milton et al., 2001.

Figure 6.6 (A) shows that the saturation level is $\sim 2 \cdot 10^5$ times more energetic than the pulse energy measured after the first undulator. Very good agreement is found between the experimental data and the simulation, in particular the slope and the location of saturation (at 17 m) are correctly predicted. In figure 6.6 (B) the electron beam is detuned to obtain an exponential gain down to the entire undulator and the saturation is not observed. In the third experiment (figure 6.6 (C)) the electron beam energy was increased to 255 MeV, so the resonant wavelength was 385 nm. Here the saturation is observed again, but the saturation power is lower than predicted. This discrepancy may be due to an electron beam trajectory error, small differences in diagnostic transmission or the particular choice of simulation parameters.

07. Conclusions

The mechanisms that can produce short pulse x-rays or gamma-rays, using laser-accelerated electrons, have been discussed. All these sources are based on the radiation from a relativistically moving charge, and if the details of the electron orbits are different for each source, the main features can be obtained using only five parameters: the relativistic factor (γ) of electrons, the number of electrons (N_e), the strength parameter of the undulator or wiggler (K), the length of a period of the undulator or wiggler (λ_u), the number of periods of the undulator or wiggler (N). Moreover, for sufficiently high-quality electrons, the incoherent radiation emitted by these sources can be amplified to coherent radiation using the FEL mechanism. Table 2 shows typical parameters and features for each source based on the use of laser-plasma interaction.

Typical features	γ	λ_u	K	N	N_e	$\hbar\omega/\hbar\omega_c$	$\theta_r(\text{mrad})$	N_r
Betatron	200	150 μm	10	3	10^9	5 keV	50	$\sim 10^9$
Conventional undulator	400	1 cm	1	100	10^8	25 eV	2.5	$\sim 10^8$
Thomson backscatterig	400	0.4 μm	1	10	10^8	650 keV	2.5	$\sim 10^7$

Table 2. Typical features for the different sources achievable with a 50 TW-class laser. Reproduced from Corde et al., 2013.

These sources can be compared, in some ways, to conventional synchrotron radiation; the main advantages provided by the laser-plasma approach are the reduced size (from kilometres to the laboratory room), the reduced cost (from billion dollars to million dollars) and the short pulse duration (from picosecond to femtosecond duration). However, compared to synchrotrons, laser-plasma based sources present significant shot to shot fluctuations in terms of photon energy, number of photons and divergence, so they can't cover a range of applications as large as synchrotron. Figure 7.1 shows the laser-plasma x-ray sources compared to other existing x-ray sources in terms of their peak brightness.

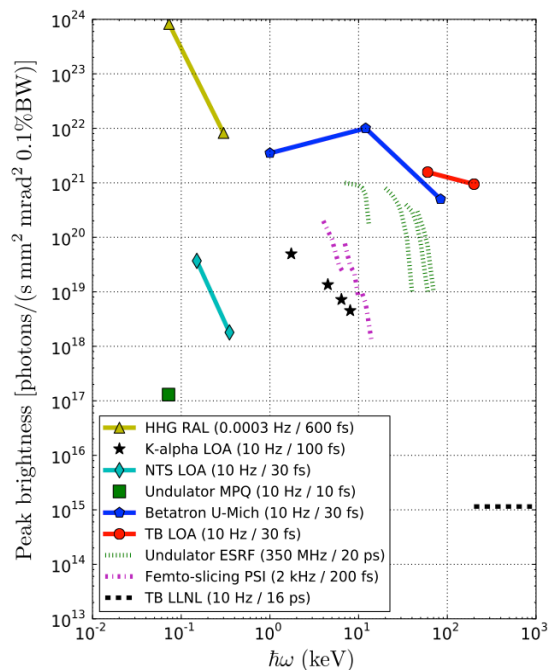


Fig. 7.1.

Peak brightness for different types of x-ray sources.

The sources are: High Harmonic Generation (HHG) from relativistic laser and overdense plasma interaction, $K\alpha$ radiation from laser-produced plasma, Nonlinear Thomson Scattering (NTS), conventional undulator radiation from laser-plasma accelerator, betatron radiation from laser-plasma accelerator, Thomson Backscattering (TB), undulator radiation from conventional accelerators, femto-slicing-based undulator radiation from conventional accelerators, Thomson Backscattering (TB) from conventional accelerators.

Reproduced from Corde et al., 2013.

Laser-plasma-based x-ray sources have competitive peak brightness; in particular, the betatron radiation and the all-optical Thomson source have high peak brightness. In the future, these sources may be improved thanks to research along the following lines:

- Betatron radiation may become brighter by using density-tailored plasmas as recently suggested by Ta Phuoc, Esarey et al., (2008). This method relies on the control of the electron orbits by varying the density, and therefore the forces acting on the electrons along the propagation. For appropriately chosen density modulation, numerical simulations show that the amplitude of the betatron oscillations r_β can be significantly increased. In an optimistic configuration described by Ta Phuoc, Esarey et al. (2008), the critical energy of the radiation can be increased by a factor of ~ 9 , the number of photons by a factor of ~ 5 , but with an increase of divergence by a factor of ~ 4 .
- The synchrotron radiation from laser-plasma accelerator combined with a conventional undulator, in the short term, will allow university-scale laboratories to access x-ray sources with angstrom wavelengths and sub-10-fs pulse duration. The main and more challenging perspective rely on the possibility to produce a free electron laser.
- Even if nonlinear Thomson scattering from the laser-plasma interaction remains a complex research topic and only a few experiments have been performed, the development of petawatt-class laser may open new perspectives for nonlinear Thomson scattering that can become a powerful x-ray source.
- The all-optically driven Thomson backscattering source, would allow one to produce tunable and nearly monochromatic radiation. This would represent a significant progress, because now, none of the existing laser-based femtosecond x-ray sources can produce monochromatic x-ray radiation. Thomson backscattering offers, as well, the possibility to produce γ -ray radiation.

Moreover, the FEL mechanism, based on laser-plasma interaction, could be the next step in the development of all these sources.

References

- Albert et al., 2010, Phys. Rev. ST Accel. Beams **13**, 070704.
- Arutyunian and Tumanian, 1963, Phys. Lett. **4**, 176.
- Ballam et al., 1969, Phys. Re. Lett. **23**, 498.
- Bonifacio et al., 1994, Phys. Re. Lett. **73**, 70.
- Bonifacio, Pellegrini and Narducci, 1984, Opt. Commun. **50**, 373.
- Brau, 1990a, *Free-Electron Lasers* (Academic, New York).
- Catravas, Esarey and Leemans, 2001, Meas. Sci. Technol. **12**, 1828.
- Chen, Maksimchuk, and Umstadter, 1998, Nature (London) **396**, 653.
- Corde et al., 2013, Rev. Mod. Phys. **85**, 1.
- Deacon et al., 1977, Phys. Rev. Lett. **38**, 892.
- Fourmaux et al., 2011a, Opt. Lett. **36**, 2426.
- Fourmaux et al., 2011b, New J. Phys. **13**, 033017
- Hafz et al., 2003, IEEE Trans. Plasma Sci. **31**, 1388.
- Hartemann et al., 2007, Phys. Rev. ST Accel. Beams **10**, 011301.
- Huang and Kim, 2007, Phys. Rev. ST Accel. Beams **10**, 034801.
- Jackson J. D., 2001, *Classical Electrodynamics*, 3rd ed. (Wiley & Sons Inc, New York).
- Kim, Xie, 1993, Nucl. Instrum. Methods Phys. Rev. Sect. A **331**, 359.
- Kondratenko and Saldin, 1980, Part. Accel. **10**, 207.
- Leemans et al., 2005, IEEE Trans. Plasma Sci. **33**, 8.
- Leemans et al., 1997, IEEE J. Quantum Electron. **33**, 1925.
- Lu, Huang, Zhou, Mori and Katsouleas, 2006, Phys. Rev. Lett. **96**, 165002.
- Lu, Huang, Zhou, Tzoufras et al., 2006, Phys. Plasmas **13**, 056709.
- Lu et al., 2007, Phys. Rev. ST Accel. Beams **10**, 061301.
- Lundh et al., 2011, Nat. Phys. **7**, 219.
- Madey, J.M., 1971, *J.Appl. Phys.* **42**, 1906-1913.
- McNeil and Thompson, 2010, Nature Photon. **4**, 814-821.
- Milburn, 1963, Phys. Rev. Lett. **10**, 75.
- Milton et al., 2001, Science **292**, 2037.
- Murphy and Pellegrini, 1985, J. Opt. Soc. Am. B **2**, 259.
- Rousse et al., 2004, Phys. Rev. Lett. **93**, 135005.
- Saldin, Schneidmiller and Yurkov, 1998, Opt. Commun. **148**, 383.
- Saldin, Schneidmiller, Yurkov, 2000, *The Physics of Free Electron Lasers* (Springer-Verlag, Berlin).
- Schlenvoigt et al., 2008b, IEEE Trans. Plasma Sci. **36**, 1773.
- Schoenlein et al., 1996, Science **274**, 236.
- Schwoerer et al., 2006, Phys. Rev. Lett. **96**, 014802.
- SLAC website: <https://news.slac.stanford.edu/features/shedding-light>.
- Ta Phuoc et al., 2003, J. Opt. Soc. Am. B **20**, 221.
- Ta Phuoc et al., 2012, Nature Photon. **6**, 308.
- Ta Phuoc, Esarey et al., 2008, Phys. Plasmas **15**, 063102.
- Ta Phuoc, Burgy, Rousseau and Rousse, 2005, Eur. Phys. J. D **33**, 301.
- Ta Phuoc, Rousse et al. 2003, Phys. Rev. Lett. **91**, 195001.
- Tomassini et al., 2005, Appl. Phys. B **80**, 419.
- Wikipedia: <http://en.wikipedia.org/wiki/X-ray>; http://it.wikipedia.org/wiki/Raggi_X.